IAS

MODELING TIME- AND DEPTH-VARYING CURRENTS AT SUPERTANK

Jane McKee Smith

U.S. Army Engineer Waterways Experiment Station, Coastal and Hydraulics Laboratory, Vicksburg, Mississippi

Ib A. Svendsen

Center for Applied Coastal Research, University of Delaware, Newark, Delaware

Submitted to Journal of Geophysical Research (Oceans)
November 12,1996

CACR-96-11

MODELING TIME- AND DEPTH-VARYING CURRENTS AT SUPERTANK

Jane McKee Smith

U.S. Army Engineer Waterways Experiment Station, Coastal and Hydraulics Laboratory, Vicksburg, Mississippi

Ib A. Svendsen

Center for Applied Coastal Research, University of Delaware, Newark, Delaware

ABSTRACT: A quasi-2D model for time-varying currents is presented. The model includes a depth-integrated, short-wave-averaged numerical model to calculate depth-integrated velocity and water surface elevation. Velocity profiles are calculated with an analytic eigenfunction solution. The model is used to simulate infragravity waves measured at the SUPERTANK Laboratory Project. Example results illustrate differences in depth and time variations inside and outside the surf zone. Outside the surf zone, most vertical variation in the cross-shore current occurs near the water surface, velocities near the surface and bottom are out of phase, and profile variation over depth is fairly symmetric. Inside the surf zone, the infragravity velocity profiles change noticeably over the time scale of the infragravity-wave period as predicted by the theory. In the inner surf zone, velocity profiles are uniform over depth.

INTRODUCTION

The quasi-3D modeling approach has been used successfully to extract steady undertow and longshore current profiles based on local wave and water level forcing [DeVriend and Stive, 1987; Svendsen and Lorenz, 1989; Svendsen and Putrevu, 1990; Sanchez-Arcilla et al., 1992; Svendsen and Putrevu, 1994]. The quasi-3D approach provides information on current variation

through the vertical without the complication of a full 3D model. The modeling approach has more recently been applied to situations with time-varying forcing. Van Dongeren et al. [1994] calculate the development of undertow and longshore current profiles from zero to steady-state forcing using a quasi-steady approach. Steady-state profiles are solved analytically using the method of Svendsen and Putrevu [1994]. Putrevu and Svendsen [1995] developed an analytic solution for time-varying infragravity wave velocity profiles in the surf zone for the special case of 2D cross-shore forcing by periodic wave groups.

The purpose of this paper is to describe a generalized model for time- and depth-dependent cross-shore flow under infragravity waves generated by random short waves. To test the model, the depth-integrated velocity and the water surface elevation are determined numerically using wave group and incident infragravity wave forcing, derived from measurements. The local water surface elevation and radiation stress gradients are then used to analytically calculate time-varying velocity profiles. No assumptions about periodicity are made with respect to the temporal variation of the forcing.

Measurements made at the SUPERTANK Laboratory Data Collection Project [Kraus and Smith, 1994; Smith and Kraus, 1995] are used to evaluate model results. The SUPERTANK project was conducted by the U.S. Army Engineer Waterways Experiment Station, Coastal Engineering Research Center, in the large wave channel at Oregon State University. This project provided the facility to measure waves and cross-shore currents on realistic beach profile shapes at prototype scale with a broad range of incident waves and bathymetries.

This paper is organized as follows: first, depth-integrated and profile components of the numerical model are described; next, the SUPERTANK measurements are briefly summarized; then, model-to-measurement comparisons are presented; and last, conclusions are stated.

NUMERICAL MODEL

Time- and depth-varying velocities are modeled in two steps. First, a numerical model of the depth-integrated continuity and momentum equations is used to calculate water surface elevations and depth-integrated velocities. Second, the output from the depth-integrated model is used to drive a local, analytic solution of cross-shore flow associated with the infragravity-wave motion. This local solution over the vertical provides the "profile" of the cross-shore flow over depth. The following sections describe the two model components.

Depth-Integrated Model

The depth-integrated model is based on the depth-integrated, short-wave-averaged equations of continuity and momentum. Several assumptions are made in the development of the model. First, since the model is applied to data taken in a long, narrow wave channel, we limit our consideration to the case of longshore homogeneity ($\partial/\partial y = 0$, where y is the longshore coordinate). This also implies zero longshore velocity, V. Second, the cross-shore component of momentum flux ($\partial U^2/\partial x$, where x is the cross-shore coordinate and U is the cross-shore short-wave-averaged velocity) is considered small and is neglected. Third, the longshore homogeneity also implies that the effect of one current component on the other (UV terms) vanishes [see Svendsen and Putrevu, 1994].

The continuity equation is

$$\frac{\partial \overline{\zeta}}{\partial t} = -\frac{\partial Q_x}{\partial x} \tag{1}$$

and the cross-shore momentum equation is

$$\frac{\partial Q_x}{\partial t} = -g(\overline{\zeta} + h_0)\frac{\partial \overline{\zeta}}{\partial x} - \frac{\partial}{\partial x}\left(\frac{S_{xx}}{\rho}\right) - \frac{\tau_{bx}}{\rho} \tag{2}$$

where Q_x is the depth-integrated volume flux in the cross-shore direction, $\overline{\zeta}$ is the infragravity wave surface elevation (the overbar denotes short-wave averaging), S_{xx} is the cross-shore radiation stress component associated with the short waves, τ_{bx} is bottom stress, h_0 is still-water depth, g is gravitational acceleration, ρ is water density, and t is time. Figure 1 provides a sketch of parameter definitions. The bottom position is assumed constant in time and, in Equations 1 and 2, the pressure variation in the infragravity waves has been assumed hydrostatic. Solution of these two equations provides information about the short-wave-averaged water level $\overline{\zeta}$ and total discharge Q_x for all x and t.

The bottom friction is parameterized as

$$\tau_{bx} = \rho \frac{f_{cw}}{\pi}(u_0 U)_{-h_0} \tag{3}$$

where f_{cw} is the bottom friction coefficient and u_0 is the cross-shore short-wave velocity amplitude. The subscript $-h_0$ indicates evaluation of parameters at the bottom. The infragravity wave velocity near the bottom is estimated using the profile model, described in the next section.

The continuity and momentum equations are solved with a second-order Predictor-Corrector scheme. The finite difference scheme is given in Appendix A. The shore boundary

condition is $Q_x = 0$. The depth at the shore boundary is approximately 0.2 m for SUPERTANK applications. The offshore boundary generates specified incident infragravity waves and absorbs reflected infragravity waves using the method of characteristics [Kobayashi et al., 1987; Van Dongeren et al., 1994].

Profile Model

The velocity profile model is based on the cross-shore momentum equation [see Svendsen and Lorenz, 1989]

$$\frac{\partial U}{\partial t} - \frac{\partial}{\partial z}\left(\nu_t \frac{\partial U}{\partial z}\right) = -g\frac{\partial \overline{\zeta}}{\partial x} - \frac{\partial(\overline{u_w^2 - w_w^2})}{\partial x} \tag{4}$$

where u_w and w_w are horizontal and vertical short-wave velocities, z is the vertical coordinate measured from the still-water level (SWL), and ν_t is eddy viscosity.

The current profiles are determined between the bottom and the mean water level (MWL). The solution requires two boundary conditions, one of which is a bottom condition that expresses that at the bottom (or strictly speaking at the top of the oscillatory bottom boundary layer), the vertical gradient of $\partial U/\partial z$ adjusts to balance the mean shear stress $\overline{\tau}_b$ developed in the bottom boundary layer. Using Equation 3, this boundary condition is expressed as

$$\rho\left(\nu_t \frac{\partial U}{\partial z}\right)_b - \frac{\rho}{\pi} f_{cw}(u_0 U)_b = 0 \tag{5}$$

[e.g., see Svendsen and Putrevu, 1990].

The second condition is specification of the shear stress at MWL that accounts for the short-wave-averaged forcing between MWL and the instantaneous water surface. This condition can be expressed as

$$\left(\frac{\partial U}{\partial z}\right)_{MWL} = \frac{\tau_s}{\rho \nu_t} \tag{6}$$

where τ_s is the time-varying surface stress, which we calculated as

$$\tau_s = \frac{\rho g H^2}{16} \tag{7}$$

based on linear theory.

For completeness, an initial condition must also be supplied, although the effect of the initial conditions dies out with time, as the solution below shows. Also, the eddy viscosity is assumed to be constant over depth.

Equation 4 is solved analytically by separation of variables, and the solution is expressed as an eigenfunction expansion. Details of the derivation are given in Appendix B. The solution for U is

$$U = \frac{\tau_s}{\rho \nu_t}\left(h_0 + z + \frac{\pi \nu_t}{f_{cw} u_w}\right) + \sum_{n=1}^{N}\left(A_n e^{-\nu_t \kappa_n^2 t} + \int_0^t F_n e^{\nu_t \kappa_n^2 (\tau - t)} d\tau\right)\cos\kappa_n(z - \bar{\zeta}) \tag{8}$$

where κ_n is a solution of the characteristic equation

$$\frac{\pi \nu_t \kappa}{f_{cw} u_w} = \frac{1}{\tan\kappa(h_0 + \bar{\zeta})} \tag{9}$$

For the special case where the forcing term, the right-hand side of Equation 4 (denoted here as f), is independent of z, the solution for F_n (eigenfunction expansion of the forcing term) is given by

$$F_n = \frac{\left(f - \frac{\partial \tau_s}{\partial t}\frac{\pi}{\rho f_{cw} u_w}\right)\sin\kappa_n(h_0 + \bar{\zeta}) + \frac{1}{\rho \nu_t}\frac{\partial \tau_s}{\partial t}\left(\frac{\cos\kappa_n(h_0 + \bar{\zeta}) - 1}{\kappa_n}\right)}{\frac{\kappa_n}{2}(h_0 + \bar{\zeta}) + \frac{1}{4}\sin 2\kappa_n(h_0 + \bar{\zeta})} \qquad (10)$$

The constant A_n is given by

$$A_n = \frac{\left(U_0 - \frac{\tau_s(0)\,\pi}{\rho f_{cw} u_w}\right)\sin\kappa_n(h_0 + \bar{\zeta}) + \frac{\tau_s(0)}{\rho \nu_t}\left(\frac{\cos\kappa_n(h_0 + \bar{\zeta}) - 1}{\kappa_n}\right)}{\frac{\kappa_n}{2}(h_0 + \bar{\zeta}) + \frac{1}{4}\sin 2\kappa_n(h_0 + \bar{\zeta})} \qquad (11)$$

where the cross-shore velocity and surface stress initial conditions are specified as $U_0(z)$ and $\tau_s(0)$ at $t = 0$.

The analytic profile model is given by Equations 8 - 11. The first term on the right-hand side of Equation 8 is a linear function of depth, and it satisfies the boundary conditions at the MWL and the bottom. The A_n term in the summation accounts for the initial conditions (U_0 and $\tau_s(0)$). This term dies out as t increases. The F_n term in Equation 8 represents the effect of the "memory" of previous forcing. This memory is inversely related to length of time prior to the present calculation time, τ-t. Thus, as we would intuitively expect, the effect of the earlier forcing in a simulation dies out as t increases. The coefficients A_n and F_n decrease as n increases. The coefficient values decrease by two to three orders of magnitude between $n = 1$ and 10, which means that only a few term are needed to give a realistic evaluation of the velocity profiles.

The profile model is also used within the depth-integrated model to define the bottom velocity, $U(-h_0)$, for calculation of the bottom friction. It is important that the forcing/resisting

functions (radiation stress and bottom friction) are the same in both models. If they are not the same, then $\overline{\zeta}$ from the depth-integrated model will not be in equilibrium with the radiation stress forcing and bottom friction in the profile model. Disequilibrium between models causes erroneous profile solutions.

SUPERTANK MEASUREMENTS

The SUPERTANK project was conducted in the large wave tank at Oregon State University during August and September 1991. The channel of the wave tank is 104 m long, 3.7 m wide, and 4.6 m deep. A 76-m-long sand beach was constructed in the channel for the project. The sand was very well graded with a median diameter of 0.22-mm. Waves were generated in the wave channel with a hydraulically-driven, hinged-flap wave board. The generator has direct digital control and is equipped to actively absorb reflected waves at the peak spectral period. Monochromatic as well as broad- and narrow-banded random waves were run with zero-moment wave heights in the range 0.2 to 1.0 m and peak spectral periods in the range 3 to 10 sec. A TMA spectral shape [Bouws et al., 1985] was used to simulate random-waves with the spectral energy density E given by

$$E(f) = \alpha g^2 f^{-5} (2\pi)^{-4} \phi \; e^{-\frac{5}{4}\left(\frac{f}{f_p}\right)^{-4}} \; \gamma^{\exp\left[\frac{\left(\frac{f}{f_p} - 1\right)^2}{2\sigma^2}\right]} \qquad (12)$$

where α is a coefficient determining the total energy level, f is frequency, f_p is peak spectral frequency, ϕ is the factor to transform the deepwater equilibrium range of the spectrum to its finite depth equivalent, γ is the spectral peakedness parameter, and $\sigma = 0.07$ for $f \leq f_p$ or $\sigma = 0.09$ for $f > f_p$.

In SUPERTANK, the cross-shore and vertical velocities were measured with 18 two-component, Marsh McBirney (model 512) electromagnetic current meters. The current meters were deployed in the nearshore from just outside the incipient breaker zone to the mid surf zone in vertical stacks of one to four current meters with vertical spacing of approximately 0.3 m and horizontal spacing of 3.7 m. The timing pulse was shared by the current meters in each vertical array to reduce cross-talk between gauges. Wave characteristics were measured throughout the channel at a spacing of 3.7 m with resistance and capacitance wave gauges. Both the wave and current signals were low-pass filtered through a fifth-order, 10-Hz Bessel filter at the input to the data acquisition system to eliminate noise and avoid aliasing. Analog wave and current data were digitized at a frequency of 16 Hz.

To separate short-wave motions from infragravity-wave motions in the measured data, a non-recursive, low-pass filter was applied. The cutoff of the filter was set to half the peak frequency of the incident waves (the peak of the long-period motion was generally 20 sec or longer). The low-pass signal included wave-group forced long waves and long waves reflected from the beach and wave generator (the generator absorbed reflected waves only at the incident peak period). The envelope of the high-pass energy was used to calculated the time-varying radiation stress, using linear theory.

Wave runs lasted between 10 and 70 minutes. Kriebel and Smith [1994] showed that long-period oscillations did occur during runs, but did not grow as a function of run length. The magnitudes of low-frequency wave heights are similar to those observed in the field.

The beach profile was surveyed before and after wave runs with an auto-tracking, infrared Geodimeter. The nominal horizontal survey spacing was 0.3 m, with finer resolution

of steep features such as bars and dunes. The profile was surveyed along the center line of the channel. Occasionally, additional lines located 0.9 m from each of the channel walls were surveyed to assess uniformity of the profile across the channel.

Wave reflection was calculated for selected SUPERTANK runs at several locations in the channel. Reflection estimates were calculated with a frequency-domain linear theory analysis technique using synoptic time series of cross-shore velocity and wave surface elevation [Hughes, 1993]. Reflection coefficients were generally 0.20 to 0.45 (all frequencies) for SUPERTANK runs. Coefficients for the low-pass frequencies were in the range 0.4 to 1.0. The reflection coefficient was strongly related to the incident peak period, with greater reflection for longer peak periods.

MODEL TO MEASUREMENT COMPARISONS

In this section, example model results for SUPERTANK Runs A0509A and A2007B are presented. These runs were selected because they include a wide range of measurement positions, wave conditions, and bathymetries.

The bathymetry for Run A0509A has an equilibrium shape, as shown in Figure 2. The positions of the current meters are shown with triangles in the figure. The short-wave parameters for Run A0509A were zero-moment wave height of 0.8 m, peak period of 3 sec, and a spectral peakedness parameter of 20, a relatively narrow spectrum. The significant infragravity wave period, determined by spectral analysis, was approximately 26 sec. This run includes measurements both outside and inside the surf zone and illustrates several typical

features of model results. Also, this is the only SUPERTANK run with a simple, non-barred bathymetry.

The bathymetry for Run A2007B has a complex barred shape, as shown in Figure 3. The multiple-bar shape was formed under a series of accretionary wave runs (low steepness waves). The positions of the current meters are again shown with triangles in the figure. The short-wave parameters for Run A2007B were zero-moment wave height of 0.7 m, peak period of 5 sec, and a spectral peakedness parameter of 100, a very narrow spectrum. The significant infragravity wave period was approximately 37 sec. This run was selected because of the very narrow spectrum and the resulting strong short-wave modulation. The current measurements were made just outside the surf zone and in the surf zone.

Model Input

To drive the wave-averaged numerical model, SUPERTANK measurements were used to provide the incident infragravity wave time series (separated from the reflected component using the linear method of Hughes [1993]) at the offshore model boundary. The offshore boundary was chosen at the most seaward of the instrument arrays ($x = 0$ m for Run A0509A and $x = 32.9$ m for Run A2007B, see Figures 2 and 3). In addition, time series of radiation stresses and the still-water depth throughout the entire model domain were used as model input. Low-pass measurements of velocity and water surface elevation were used to evaluate the model at the locations of the instrument arrays. In all the calculations, the variation of the short-wave radiation stress is one of the important forcing contributions to the cross-shore velocities. For application of the model to SUPERTANK measurements, the radiation stress variation was calculated from the measured envelope of short-wave amplitude squared, using linear wave

theory. The wave gauge spacing does not resolve the region of incipient breaking well enough to provide the input required for model calculations, and unfortunately, we have limited theoretical knowledge about the transformation and breaking of short-wave groups that can be used to supplement the measurements. Therefore, the envelope of wave amplitude squared was linearly interpolated between gauges and used to estimate the radiation stress variation.

The incident infragravity-wave time series (the offshore boundary condition for the model) for SUPERTANK were calculated using the method developed by Hughes [1993]. This method is based on a linear technique that separates the incident and reflected waves using co-located measurements of velocity and water surface elevation. A bottom friction coefficient of $f_{cw} = 0.01$ was used.

The eddy viscosity is parameterized using the expression given by Svendsen and Putrevu [1994]

$$\nu_t = \begin{cases} 0.01 h_0 \sqrt{g h_0} & \text{inside surf zone} \\ \left[0.8 \left(\dfrac{h_0}{h_b} \right)^{-4} + 0.2 \right] \nu_{tb} & \text{outside surf zone} \end{cases} \qquad (13)$$

where h_b is the depth at incipient wave breaking and $\nu_{tb} = 0.01\ h_b\ (g\ h_b)^{1/2}$. In the absence of more detailed information, the breaking depth is estimated as $h_b = H_{mo}/0.8$, where H_{mo} is the incident zero-moment wave height. For simplicity, the radiation stresses are calculated from linear theory, which implies that one-third of the radiation stress is applied as a surface stress at MWL and the remaining two-thirds is applied uniformly over depth, as indicated by Equation 7. The gradient in the infragravity water surface elevation, which is also used as forcing, is calculated from the output of the depth-integrated model.

Depth-Integrated Results

For Run A0509A, the region modeled extends from a depth of 2.4 m to 0.2 m. The cross-shore grid spacing was 0.91 m with 57 grid cells, and the time step used was 0.125 sec or approximately 24 time steps per short-wave peak period. For Run A2007B, the region modeled extends from a depth of 0.8 m to 0.1 m. The cross-shore grid spacing was 0.61 m with 37 grid cells, and the time step used was again 0.125 sec or 40 time steps per short-wave peak period. The time step was chosen to be a multiple of the sampling time increment of 0.0625 sec. The grid spacings were selected so measurement points aligned with grid cells and the Courant criterion was met. The initial condition specified was $Q_x = 0$ m^2/sec and $\overline{\zeta} = 0$ m throughout the domain. The incident infragravity wave forcing at the offshore boundary and the radiation stress forcing throughout the domain were started from zero and linearly increased to their measured values over the first 500 time steps.

Example results for the infragravity-wave water surface elevation and depth-integrated velocities for Run A0509A are given in Figures 4 and 5, respectively, and for Run A2007B in Figures 6 and 7, respectively. The figures show time series results for four x locations. The solid lines are the wave and current measurements and the dashed lines are the model results. Positive velocities are directed onshore and negative velocities are offshore. The measured velocities are averaged over all gauges below the still-water level.

A major weakness in the present comparison is the difficulty establishing the correct mean short-wave forcing (the forcing averaged over an entire run). The mean of the measured water surface elevations (time average of $\overline{\zeta}$ taken over the entire run, also referred to as setup or setdown) ranged from -0.013 to 0.008 m for the two runs. The computed mean elevations

ranged from -0.016 to 0.056 m. Thus, the model did not accurately reproduce the mean water elevations. The model-predicted setdown is approximately twice the measured values, although the maximum calculated setdown is about equal to the measured value (the model-predicted point is approximately 15 m seaward of the measured point for Run A0509A). For Run A2007B where all gauges except the most seaward is in the surf zone, the setup calculated at the gauge locations is significantly larger than the measurements. The errors are linked to inaccuracies in the calculation of the mean radiation stress. The setdown and setup are driven by the gradients in the mean radiation stress (caused by wave shoaling and breaking). The region of incipient breaking is not well captured in the measurements due to the fairly coarse spacing of the wave gauges, and thus the wave height variation in the incipient breaker zone and the mean radiation stress forcing are also not well captured. Also contributing to these inaccuracies is that linear theory was used to calculate radiation stress, and it has been shown to overpredict setup and does not account for the transition region between incipient breaking and wave setup [Svendsen, 1984]. Though the theory remains inaccurate through the surf zone, the major error source is the significant overprediction of the radiation stress at the break point. This sets the stage for generally too large radiation stress gradients through the entire surf zone.

The average root-mean-square (rms) error relative to the measured data for the water surface elevations is 0.040 m for Run A0509a and 0.044 m for Run A2007B. For comparison, the maximum amplitude of the infragravity surface elevation was approximately $\pm$ 0.15 m for both runs. The errors increase in the shallowest depths. The reason for the increase in error at shallow depths is three-fold: (a) again, the linear radiation stress calculations are less accurate in shallower depths as the waves become more nonlinear and have shapes that are less

sinusoidal, (b) the bottom topography varies in the shallower depths and as the sand depth at the gauge (the shallow wave gauges extend into the sand bed) changes during the run, the gauge offset (the offset is calculated as the gauge reading prior to wave action at the beginning of the run) can also change, and (c) the error in setup and setdown (the average value of $\overline{\zeta}$ over a run) increases substantially in shallow water.

Up to 55 percent of the rms error accounts for the mean errors previously discussed. Removing the mean reduced the average rms error to 0.035 and 0.031 m for Runs A0509A and A2007B, respectively.

The mean measured cross-shore velocities ranged from -0.015 to -0.069 m/sec and the modeled velocities were zero, as would be expected from a depth-averaged model with no net inflow or outflow. The depth-averaged measured mean velocities do show a net offshore flow or undertow. This is due to the fact that all measurements used in the average were below the still-water level. Data from gauges shown in Figures 2 and 3 that were at or above the still-water level tended to be unreliable and were neglected. The measurements are capturing, to varying degrees depending on measurement elevation, the return flow from the wave-driven mass transport.

Figures 8 and 9 show example spectra of the measured (solid line) and modeled (dashed line) water surface elevations and depth-integrated velocities, respectively. The spectra have 20 degrees of freedom, and the means have been removed. The spectra show generally good agreement between the model and measurements. Both the total energy in the spectra and the spectral shape given by the model compare reasonably well with the measurements, with two exceptions. First, at $x = 32.9$ m (the boundary condition for Run A2007B), the modeled water

surface elevation spectrum differs significantly from the measurement. This indicates that either the separation of the incident and reflected infragravity waves used in the boundary condition was inaccurate, which would not be surprising in this region near incipient breaking, or the reflected wave component calculated in the model is inaccurate. Second, in the shallower depths, the model depth-integrated velocity spectra have much less energy than the measured spectra.

Velocity Profile Results

Results for the horizontal velocity profiles were determined using 10 eigenfunctions and specifying output at 21 locations over the vertical. As discussed previously, contribution from the eigenfunctions decrease rapidly with increasing n, so contributions from $n > 10$ are negligible. The initial condition was $U = 0$ m/sec for all x and z. Example results are shown in Figures 10 - 17. In the Figures the solid line is the output from the profile model, the dashed line is the computed depth-integrated velocity, and the symbols are measurements. The vertical axis is the dimensionless depth $Z = (h_0 + z)/h_0$. For Run A0509A, the profiles in Figures 10 - 12 are well outside the surf zone at $x = 25.6$ m, 36.6 m and 40.2 m, and the profiles in Figure 13 are in the outer surf zone at $x = 43.9$ m. For Run A2007B, the profiles in Figure 14 are just outside the surf zone at $x = 36.6$ m, and the profiles in Figures 15 - 17 are in the surf zone at $x = 37.2$ m, 40.2 m, and 43.9 m. The six panels in each figure represent six "snap shots" in time. Figures 18 and 19 are overlays of calculated velocity profiles at 3-sec time increments from $t = 250$ - 500 sec for Runs A0509A and A2007B, respectively.

Outside the surf zone, typical velocity profiles exhibit three characteristics: (a) the greatest velocity variation occurs near the surface, (b) the velocities near the surface and bottom

surface elevation spectrum differs significantly from the measurement. This indicates that either the separation of the incident and reflected infragravity waves used in the boundary condition was inaccurate, which would not be surprising in this region near incipient breaking, or the reflected wave component calculated in the model is inaccurate. Second, in the shallower depths, the model depth-integrated velocity spectra have much less energy than the measured spectra.

Velocity Profile Results

Results for the horizontal velocity profiles were determined using 10 eigenfunctions and specifying output at 21 locations over the vertical. As discussed previously, contribution from the eigenfunctions decrease rapidly with increasing n, so contributions from $n > 10$ are negligible. The initial condition was $U = 0$ m/sec for all x and z. Example results are shown in Figures 10 - 17. In the Figures the solid line is the output from the profile model, the dashed line is the computed depth-integrated velocity, and the symbols are measurements. The vertical axis is the dimensionless depth $Z = (h_0 + z)/h_0$. For Run A0509A, the profiles in Figures 10 - 12 are well outside the surf zone at $x = 25.6$ m, 36.6 m and 40.2 m, and the profiles in Figure 13 are in the outer surf zone at $x = 43.9$ m. For Run A2007B, the profiles in Figure 14 are just outside the surf zone at $x = 36.6$ m, and the profiles in Figures 15 - 17 are in the surf zone at $x = 37.2$ m, 40.2 m, and 43.9 m. The six panels in each figure represent six "snap shots" in time. Figures 18 and 19 are overlays of calculated velocity profiles at 3-sec time increments from $t = 250$ - 500 sec for Runs A0509A and A2007B, respectively.

Outside the surf zone, typical velocity profiles exhibit three characteristics: (a) the greatest velocity variation occurs near the surface, (b) the velocities near the surface and bottom

are out of phase, and (c) the profile variation over depth is relatively symmetric about $U =$ 0 m/sec (mean vertical variation is near zero). These characteristics are illustrated in Figures 10 - 12 and 18 - 19. The velocity profiles are nearly uniform over the lower two-thirds of the depth. Near the surface, the velocity magnitude is greater and the direction is often opposite that of the lower part of the water column. Typically, in the offshore region the time-varying surface stress is the dominant forcing. Since the mean forcing is small, the profiles are approximately symmetric about $U = 0$ m/sec. The water depth is relatively deep, so the surface stress impact is exhibited with higher velocities near the surface.

Inside the surf zone (Figures 13-17), the various forcing contributions are much stronger due to the rapid variation in short-wave quantities caused by wave breaking, and the uncertainties of the predicted forcing are more significant. Hence in several cases the model fails to predict the measured results. However, in Figures 13, 14, and 15, there are rapid shifts of the type predicted by the theory that occur in the vertical gradient of the measured velocities. Thus several profiles (see, e.g., Figure 13 at $t = 675$ and 684 sec and Figure 15 at $t = 129$ and 132 sec) have velocities near the surface that are more seaward oriented than lower in the water column, inspite of the tendency the steady undertow would have to force a profile to curve toward the shore near the surface. And, a short while later the picture has shifted to undertow-type profiles in those examples, as predicted. According to the theory, the behavior of the infragravity-wave velocity profiles depends strongly on the phase difference between the surface forcing and the depth uniform forcing. Whereas the surface forcing is entirely caused by the variation in the short-wave motion (radiation stress variations due to groupiness), the depth uniform forcing is created by the contribution of the same radiation stress variation and the total

pressure gradients in the infragravity-wave motion. Figures 18 and 19 show that the velocity profiles are relatively vertical for positive (onshore) mean velocities and more parabolic for negative (offshore) mean velocities. In the inner surf zone, model results and measurements show little velocity variation over the vertical as the time-varying, depth-uniform forcing (particularly the surface elevation gradient associated with the infragravity motion itself) becomes dominant.

The average rms error in the calculated velocities relative to the measurements is 0.14 m/sec for Run A0509A and 0.20 m/sec for Run A2007B. For comparison, the maximum amplitude of the infragravity velocities was approximately $\pm$ 1.0 m/sec. Considering only the time-varying velocity, the rms error decreases slightly for Run A0509A and decreases about 20 percent for Run A2007B. As discussed under the depth-integrated model results, the mean velocities are not in general well represented in the model. The error is uncorrelated with elevation in the water column, but error does increase in the surf zone.

Putrevu and Svendsen [1995] identified three dimensionless parameters that together describe infragravity wave velocity profiles: βh which determines the depth to which the effect of the surface and bed shear stresses are felt (where $\beta = (\omega/(2\ \nu_t))^{0.5}$, ω is the infragravity wave frequency, and h is water depth); δ which is the relative phase between the surface stress and depth-uniform forcing; and $T_s\ \beta/(\rho\ F_a)$ which is the relative magnitude of the surface stress to the depth-uniform forcing, where T_s and F_a are the amplitudes of the surface stress and depth-uniform forcing, respectively. A summary of estimated parameter values for the SUPERTANK results are shown in Figures 20 and 21. The parameters are estimated using an infragravity wave peak frequency of 0.039 Hz (infragravity wave peak period of 25.6 sec) for Run A0509A

and 0.027 Hz (peak period of 37.0 sec) for Run A2007B, though the peak frequencies varied somewhat across shore.

The interpretation of the parameters values illustrates the mechanisms behind the trends discussed previously. The larger value of βh outside the surf zone implies that surface stress forcing will impact a smaller percentage of the water column than at locations inside the surf zone where βh is smaller. It also implies that the greatest vertical variation will be near the surface. For Run A0509A (Figure 20), βh varies from 10 offshore to 1 in the surf zone, which is reflected in the difference between the profiles with greater variations near the surface in the offshore (large βh) and profiles with an almost uniform variation in magnitude over depth in the surf zone (small βh). For Run A2007B (Figure 21), βh is relatively constant (1.5 to 1.0), and the profile variation over depth is similar to the surf zone profiles of Run A0509A which have similar values of βh.

For both Runs A0509A and A2007B, $\delta \approx \pi$ outside the surf zone and in the outer surf zone. Longuet-Higgins and Stewart [1964] found that for steady-state forcing, $\overline{\zeta}$ tends to be negative below high waves and positive under low waves, which means that radiation stress (and its gradient) is π out of phase with the infragravity-wave surf elevation (and its gradient). The depth-uniform forcing includes both the depth-uniform part of the radiation stress gradient and the pressure gradient due to the infragravity waves. Thus, since the latter will usually dominate the depth-uniform forcing, it is expected that the surface stress forcing (also resulting from the radiation stress gradient) and depth-uniform forcing will be approximately π out of phase. In the surf zone ($x = 40$ m for Run A0509A and the inner surf zone, $x = 45$ m, for Run A2007B) δ decreases to $\pi/2$. Thus, in the surf zone, the surface stress and depth-uniform forcing are

closer to being in phase. The decease in δ in the surf zone indicates that the upper and lower portions of the velocity profile should also be less out of phase, as seen previously.

The last parameter, $T_s\,\beta/(\rho\,f_a)$, shows that the forcing outside the surf zone tends to be surface stress dominated ($T_s\,\beta/(\rho\,f_a) > 0.7$), while in the surf zone the forcing is balanced or depth-uniform forcing is relatively stronger. The reason is that the surface stress forcing is caused by the variation of the short-wave motion with time and as we move further into the surf zone the short-wave height decreases and with it its time variation. In contrast the long-wave amplitude (and hence its surface gradient) increases shoreward which creates the large depth-uniform forcing due to the pressure gradients. In general, surface stress dominated profiles are parabolic in shape and depth-uniform dominated profiles are linear and vertical in shape. In the relatively long, flat inner surf zone of Run A2007B the depth-uniform forcing dominates ($T_s\,\beta/(\rho\,f_a) < 0.7$, see Figure 19, $x = 50$ m). Here, the short-wave energy is dissipated and the velocity profile shape is nearly uniform over depth.

CONCLUSIONS

This paper presents a model for time- and depth-varying currents. The model consists of a depth-integrated numerical component that provides mean velocities and surface elevations and an analytic component that determines the infragravity-wave velocity profiles. The model was applied to wave and current measurements from the SUPERTANK Laboratory Project. Model comparisons to the laboratory measurements showed good agreement in the time-varying velocity and water surface elevation, but poor results for mean values.

The model results for SUPERTANK exhibited the following characteristics:

(a) outside the surf zone

- The greatest velocity variation occurred near the surface (large βh and surface stress dominating)
- Velocities near the surface and the bottom were out of phase with the surface velocities
- Profile variation over depth was fairly symmetric about $U = 0$ m/sec (small mean forcing)

(b) inside the surf zone

- The mean undertow profile is the dominant feature (mean forcing is dominating)
- The infragravity velocity profiles show variations that are in accordance with changes over a time scale of the infragravity-wave period
- The time variation of the velocity is fairly constant over depth (small βh and small δ)
- In the inner surf zone, the velocity profile is uniform over depth (small surface stress forcing)

Considering the simplicity of some of the input estimates used, the results confirm that the model represents the mechanisms that generate the infragravity velocity profiles relatively well. This indicates that, in general, infragravity wave velocities may be far from uniform over depth, in contrast to what one should expect from the long-wave nature of these waves.

APPENDIX A. SECOND-ORDER PREDICTOR-CORRECTOR SCHEME

The predictor step is:

$$\overline{\zeta}_i^* = \overline{\zeta}_i^n + \frac{\Delta t}{2}\left(3E_i^n - E_i^{n-1}\right) \tag{A1}$$

$$Q_{x_i}^* = Q_{x_i}^n + \frac{\Delta t}{2}\left(3F_i^n - F_i^{n-1}\right) \tag{A2}$$

where the i subscript represents the x grid index where the variable is evaluated, the superscripts represent the time step (e.g., n and n-1) when the variable is evaluated, the * superscript represents an intermediate time step, Δt is the time step, and

$$E = -\left(\frac{\partial Q_x}{\partial x}\right) \tag{A3}$$

$$F = -g(\overline{\zeta} + h_0)\frac{\partial \overline{\zeta}}{\partial x} - \frac{\partial}{\partial x}\left(\frac{S_{xx}}{\rho}\right) - \frac{\tau_{bx}}{\rho} \tag{A4}$$

The spatial derivatives are calculated with second-order, central finite differences. At the offshore grid boundary, second-order forward differences are applied, and at the shore boundary, second-order backward differences are applied.

The corrector step is:

$$\overline{\zeta}_i^{n+1} = \overline{\zeta}_i^n + \frac{\Delta t}{12}\left(5E_i^* + 8E_i^n - E_i^{n-1}\right) \tag{A5}$$

$$Q_{x_i}^{n+1} = Q_{x_i}^n + \frac{\Delta t}{12}\left(5F_i^* + 8F_i^n - F_i^{n-1}\right) \tag{A6}$$

The boundary conditions applied in the model include a no-flux condition at the beach (no flow into the beach) and an absorbing-generating offshore boundary condition.

APPENDIX B. SOLUTION FOR VELOCITY PROFILE

Equation 4 is solved using separation of variables and the Sturm-Liouville approach. The solution is determined in two parts: u which satisfies the boundary conditions in z, and v which is broken into a homogeneous solution and a particular solution, v_p.

First, a partial solution $u(z,t)$ is chosen which satisfies the boundary conditions in z

$$u(z,t) = \frac{\tau_s}{\rho \nu_t}\left(h_0 + z + \frac{\pi \nu_t}{f_{cw} u_o}\right) \tag{B1}$$

The solution for Equation 4 then becomes

$$U(z,t) = u(z,t) + v(z,t) \tag{B2}$$

The governing equation for v is

$$\frac{\partial v}{\partial t} - \nu_t \frac{\partial^2 v}{\partial z^2} = f^*(t) \tag{B3}$$

where

$$f^*(t) = f(t) - \frac{\partial u}{\partial t} = f(t) - \frac{1}{\rho \nu_t}\frac{\partial \tau_s}{\partial t}(h_0 + z + \frac{\pi \nu_t}{f_{cw} u_o}) \qquad \textbf{(B4)}$$

and $f(t)$ is defined as the right-hand side of Equation 4. The boundary conditions for Equation B3 are then given by the homogeneous expression

$$\frac{\partial v}{\partial z} = 0 \quad \text{at} \quad z = \overline{\zeta} \qquad \textbf{(B5)}$$

and

$$\rho \nu_t \frac{\partial v}{\partial z} - \frac{\rho}{\pi} f_{cw} u_o v = 0 \quad \text{at} \quad z = -h_0 \qquad \textbf{(B6)}$$

The homogeneous equation for v

$$\frac{\partial v}{\partial t} - \nu_t \frac{\partial^2 v}{\partial z^2} = 0 \qquad \textbf{(B7)}$$

is solved by the method of separation of variables, in the form $v = Z(z)T(t)$. Substituting the assumed form of v into Equation B7 gives the two equations

$$\frac{d^2 Z}{dz^2} + \kappa^2 Z = 0 \qquad \textbf{(B8)}$$

$$\frac{dT}{dt} + \nu_t \kappa^2 T = 0 \qquad \textbf{(B9)}$$

for Z and T. The general solution for v then becomes

$$v = ZT = (A\cos\kappa\xi + B\sin\kappa\xi)e^{-\nu_t \kappa^2 t} + C + D\xi \qquad \textbf{(B10)}$$

where $\xi = z - \overline{\zeta}$.

The boundary conditions are applied to determine the integration constants. At $\xi = 0$,

$$\frac{\partial v}{\partial \xi} = 0 = (B\kappa)e^{-\nu_t \kappa^2 t} + D \tag{B11}$$

Since the first and second term on the right-hand side of Equation B11 are linearly independent, $B = D = 0$. At $\xi = -(h_0 + \overline{\zeta})$ we have

$$\rho \nu_t \frac{\partial v}{\partial \xi} - \frac{\rho}{\pi} f_{cw} u_o v = 0 \tag{B12}$$

or

$$\rho \nu_t(-A\kappa \sin\kappa\xi \; e^{-\nu_t \kappa^2 t}) - \frac{\rho}{\pi} f_{cw} u_o (A\cos\kappa\xi \; e^{-\nu_t \kappa^2 t} + C) = 0 \tag{B13}$$

Again, due to linear independence of the solution $C = 0$, which gives the characteristic equation for κ

$$\frac{\pi \nu_t \kappa}{f_{cw} u_o} = \frac{1}{\tan\kappa(h_0 + \overline{\zeta})} \tag{B14}$$

The general homogeneous solution for v is then

$$v(z,t) = \sum_{n=1}^{N} A_n \cos\kappa_n(z-\overline{\zeta}) \; e^{-\nu_t \kappa_n^2 t} \tag{B15}$$

To determine a particular solution for v, we first express the forcing term, f, as an eigenfunction expansion. We define

$$F_n(t) = \frac{\langle f - \frac{1}{\rho \nu_t}\frac{\partial \tau_s}{\partial t}(h_0 + z + \frac{\pi \nu_t}{f_{cw} u_o}),\ \cos\kappa_n(z - \bar{\zeta}) \rangle}{\langle \cos\kappa_n(z - \bar{\zeta}),\ \cos\kappa_n(z - \bar{\zeta}) \rangle} \tag{B16}$$

where the triangular brackets represent the inner product of the two enclosed functions. Then

$$f^*(t) = \sum_{n=1}^{N} F_n(t)\ \cos\kappa(z - \bar{\zeta}) \tag{B17}$$

We determine the particular solution v_p by assuming v_p can be written in the form

$$v_p = \sum_{n=1}^{N} B_n(t)\ \cos\kappa_n(z - \bar{\zeta})\ e^{-\nu_t \kappa_n^2 t} \tag{B18}$$

Substituting into Equation B3 yields

$$\begin{aligned} &\frac{\partial B_n}{\partial t}\cos\kappa_n(z - \bar{\zeta})e^{-\nu_t\kappa_n^2 t} - \nu_t\kappa_n^2 B_n\cos\kappa_n(z - \bar{\zeta})e^{-\nu_t\kappa_n^2 t} \\ &\quad + \nu_t\kappa^2 B_n\cos\kappa_n(z - \bar{\zeta})e^{\nu_t\kappa_n^2 t} = F_n\cos\kappa_n(z - \bar{\zeta}) \end{aligned} \tag{B19}$$

which simplifies to

$$\frac{\partial B_n}{\partial t}e^{-\nu_t\kappa_n^2 t} = F_n \tag{B20}$$

or

$$B_n = \int_0^t F_n e^{\nu_t\kappa_n^2 \tau}\, d\tau \tag{B21}$$

Substituting Equation B21 into B18 provides the particular solution

$$v_p = \sum_{n=1}^{N} \int_0^t F_n e^{\nu_t \kappa_n^2 (\tau - t)} d\tau \cos\kappa_n (z - \zeta_t) \tag{B22}$$

The complete solution for v is the sum the homogeneous and the particular solutions

$$v = \sum_{n=1}^{N} [A_n e^{-\nu_t \kappa_n^2 t} + \int_0^t F_n e^{\nu_t \kappa_n^2 (\tau - t)} d\tau] \cos\kappa_n (z - \bar{\zeta}) \tag{B23}$$

where the A_n terms represent the effect of the initial conditions. Finally, returning to Equation B2, the solution for the cross-shore velocity profile is the sum of Equations B1 and B23, i.e.,

$$U = \frac{\tau_s}{\rho \nu_t}\left(h_0 + z + \frac{\pi \nu_t}{f_{cw} u_o}\right) + \sum_{n=1}^{N} [A_n e^{-\nu_t \kappa_n^2 t} + \int_0^t F_n e^{\nu_t \kappa_n^2 (\tau - t)} d\tau] \cos\kappa_n (z - \bar{\zeta}) \tag{B24}$$

We consider the case of the forcing term f in Equation B3 independent of z (the first term on the right hand side of Equation 4 is independent of z, and the second term has a weak dependence in shallow water). The solution for F_n, for the special case where f is not a function of z (which is often a good approximation), is given by the solution of Equation B16

$$F_n = \frac{-\left(f - \frac{\partial \tau_s}{\partial t} \frac{\pi}{\rho f_{cw} u_o}\right) \sin\kappa_n (h_0 + \bar{\zeta}) + \frac{1}{\rho \nu_t} \frac{\partial \tau_s}{\partial t}\left(\frac{\cos\kappa_n (h_0 + \bar{\zeta}) - 1}{\kappa_n}\right)}{\frac{\kappa_n}{2}(h_0 + \bar{\zeta}) + \frac{1}{4}\sin 2\kappa_n (h_0 + \bar{\zeta})} \tag{B25}$$

Similarly, the solution for A_n is given by

$$A_n = \frac{(U_o - \frac{\tau_s(0)\,\pi}{\rho f_{cw} u_o})\sin\kappa_n(h_0 + \bar{\zeta}) + \frac{\tau_s(0)}{\rho\,\nu_t}\left(\frac{\cos\kappa_n(h_0 + \bar{\zeta}) - 1}{\kappa_n}\right)}{\frac{\kappa_n}{2}(h_0 + \bar{\zeta}) + \frac{1}{4}\sin 2\kappa_n(h_0 + \bar{\zeta})} \qquad \text{(B26)}$$

where U_o in the initial condition. In practice, the effect of the initial condition dies out as the exponential factor in the A_n-term in Equation B23 indicates.

ACKNOWLEDGMENTS

Permission was granted by the Office, Chief of Engineers, U.S. Army Corps of Engineers, to publish this information. This research was supported by the USAE Waterways Experiment Station, Laboratory Discretionary Research and Development Program (JMS) and by Sea Grant, Contract NA56RG0147 (IAS).

REFERENCES

Bouws, E., H. Gunther, W. Rosenthal, and C. L. Vincent, Similarity of the wind wave spectrum in finite depth water; 1. spectral form, *J. Geophys. Res.*, 90(C1), 975-986, 1985.

DeVriend, H., and M. J. F. Stive, Quasi-3D modelling of nearshore currents, *Coastal Engrg.*, 11, 565-601, 1987.

Hughes, S. A., Laboratory wave reflection analysis using co-located gages, *Coastal Engrg.*, 20, 223-247, 1993.

Kobayashi, N., A. K. Otta, and I. Roy, Wave reflection and run-up on rough slopes, *J. Wtrwy. Port, Coastal, and Ocean Engrg.*, 113(3), 282-298, 1987.

Kraus, N. C., and J. M. Smith, SUPERTANK Laboratory Data Collection Project, Volume I: Main text, 274 pp., Technical Report CERC-94-3, U.S. Army Engineer Waterways Experiment Station, Vicksburg, MS, 1994.

Kriebel, D. L., and J. M. Smith, Wave transformation measurements at SUPERTANK, *Proc., Coastal Dynamics'94*, 233-247, 1994.

Longuet-Higgins, M. S., and R. W. Stewart, Radiation stresses in water waves; a physical discussion, with applications, *Deep-Sea Res.*, 11, 529-562, 1964.

Putrevu, U., and I. A. Svendsen, Infragravity velocity profiles in the surf zone, *J. Geophys. Res.*, 100(C8), 16,131-16,142, 1995.

Roach, P. J., *Computational Fluid Dynamics*, 446 pp., Hermosa Publishers, Albuquerque, New Mexico, 1982.

Sanchez-Arcilla, A., F. Collado, and A. Rodriguez, Vertically varying velocity field in Q-3D nearshore circulation, *Proc., 23rd Coastal Engrg. Conf.*, ASCE, 2811-2824, 1992.

Smith, J. M., and N. C. Kraus, SUPERTANK Laboratory Data Collection Project, Volume II: Appendices A-I, 241 pp., Technical Report CERC-94-3, U.S. Army Engineer Waterways Experiment Station, Vicksburg, MS, 1995.

Svendsen, I. A., Wave heights and set-up in the surf zone, *Coastal Engrg.*, 8(4), 303-329, 1984.

Svendsen, I. A., and R. S. Lorenz, Velocities in combined undertow and longshore currents, *Coastal Engrg.*, 13, 55-79, 1989.

Svendsen, I. A., and U. Putrevu, Nearshore circulation with 3-d profiles, *Proc., 22nd Coastal Engrg. Conf.*, ASCE, 241-254, 1990.

Svendsen, I. A., and U. Putrevu, Nearshore mixing and dispersion, *Proc. R. Soc. Lond.*, 445, 561-576, 1994.

Van Dongeren, A. R., R. E. Sancho, I. A. Svendsen, and U. Putrevu, SHORECIRC: a quasi 3-d nearshore model, *Proc., 24th Coastal Engrg Conf.*, ASCE, 2741-2754, 1994.

J. M. Smith, U.S. Army Engineer Waterways Experiment Station, CEWES-CR-P, 3909 Halls Ferry Road, Vicksburg, MS 39180-6199, USA, jm.smith@cerc.wes.army.mil

I. A. Svendsen, Center for Applied Coastal Research, University of Delaware, Newark, DE 19716, USA, ias@coastal.udel.edu

FIGURE CAPTIONS

Figure 1. Parameter definition
Figure 2. Bathymetry and current meter positions for Run A0509A
Figure 3. Bathymetry and current meter positions for Run A2007B
Figure 4. Infragravity surface elevations (solid -- measured, dashed -- calculated) for Run A0509A
Figure 5. Depth-integrated velocities (solid -- measured, dashed -- calculated) for Run A0509A for Run A0509A
Figure 6. Infragravity surface elevations (solid -- measured, dashed -- calculated) for Run A0509A for Run A2007B
Figure 7. Depth-integrated velocities (solid -- measured, dashed -- calculated) for Run A0509A for Run A2007B
Figure 8. Spectra of infragravity-wave water surface elevations for Run A2007B
Figure 9. Spectra of infragravity-wave depth-integrated velocities for Run A2007B
Figure 10. Velocity profiles at $x = 25.6$ m (solid line -- profile model, dashed line -- depth-integrated model, symbols -- measurements) for Run A0509A
Figure 11. Velocity profiles at $x = 36.6$ m (solid line -- profile model, dashed line -- depth-integrated model, symbols -- measurements) for Run A0509A
Figure 12. Velocity profiles at $x = 40.2$ m (solid line -- profile model, dashed line -- depth-integrated model, symbols -- measurements) for Run A0509A
Figure 13. Velocity profiles at $x = 43.9$ m (solid line -- profile model, dashed line -- depth-integrated model, symbols -- measurements) for Run A0509A
Figure 14. Velocity profiles at $x = 36.6$ m (solid line -- profile model, dashed line -- depth-integrated model, symbols -- measurements) for Run A2007B
Figure 15. Velocity profiles at $x = 37.2$ m (solid line -- profile model, dashed line -- depth-integrated model, symbols -- measurements) for Run A2007B
Figure 16. Velocity profiles at $x = 40.2$ m (solid line -- profile model, dashed line -- depth-integrated model, symbols -- measurements) for Run A2007B
Figure 17. Velocity profiles at $x = 43.9$ m (solid line -- profile model, dashed line -- depth-integrated model, symbols -- measurements) for Run A2007B
Figure 18. Calculated profiles for Run A0509A, $t = 500$-750 sec
Figure 19. Calculated profiles for Run A2007B, $t = 500$-750 sec
Figure 20. Relative strength of surface stress and depth-uniform forcing (solid line) and βh (dashed line) and relative phase of surface stress and depth-uniform forcing for Run A0509A
Figure 21. Relative strength of surface stress and depth-uniform forcing (solid line) and βh (dashed line) and relative phase of surface stress and depth-uniform forcing for Run A2007B

MODELING TIME- AND DEPTH-VARYING CURRENTS AT SUPERTANK

Jane McKee Smith and Ib A. Svendsen

KEYWORDS

Currents
Depth variation
Infragravity waves
Laboratory measurements
Numerical model
Quasi-2-D
SUPERTANK
Time variation
Undertow
Wave groups

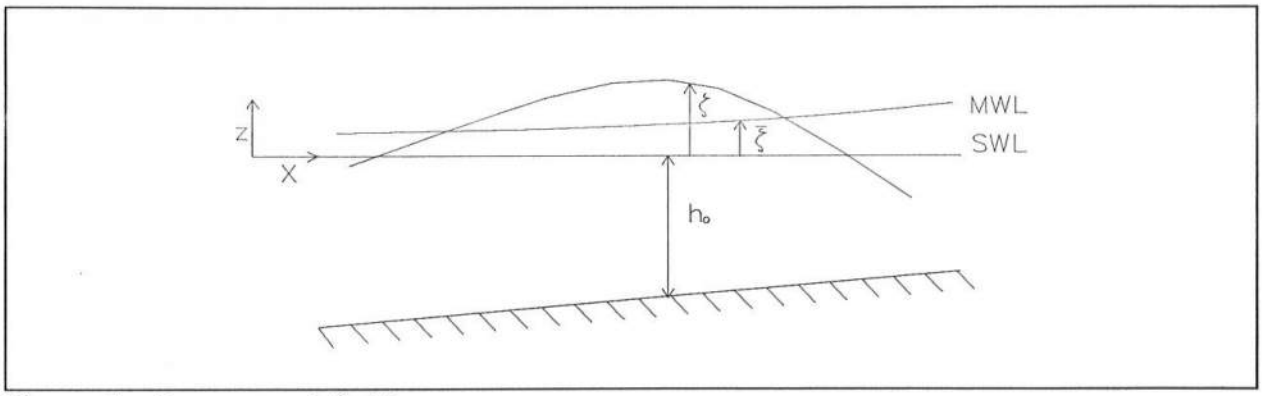

Figure 1. Parameter definition

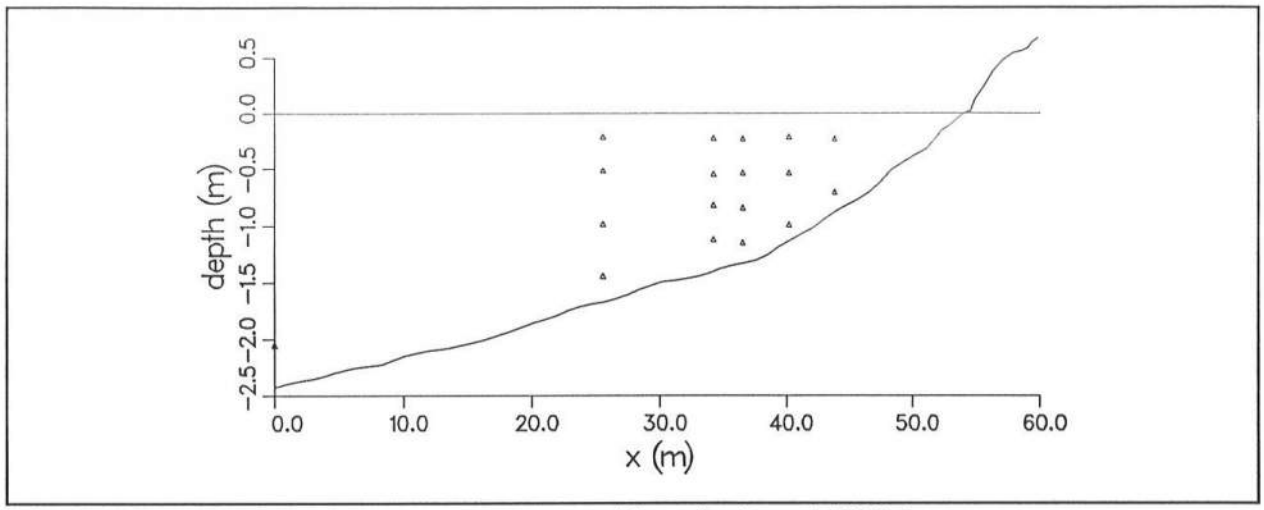

Figure 2. Bathymetry and current meter positions for Run A0509A

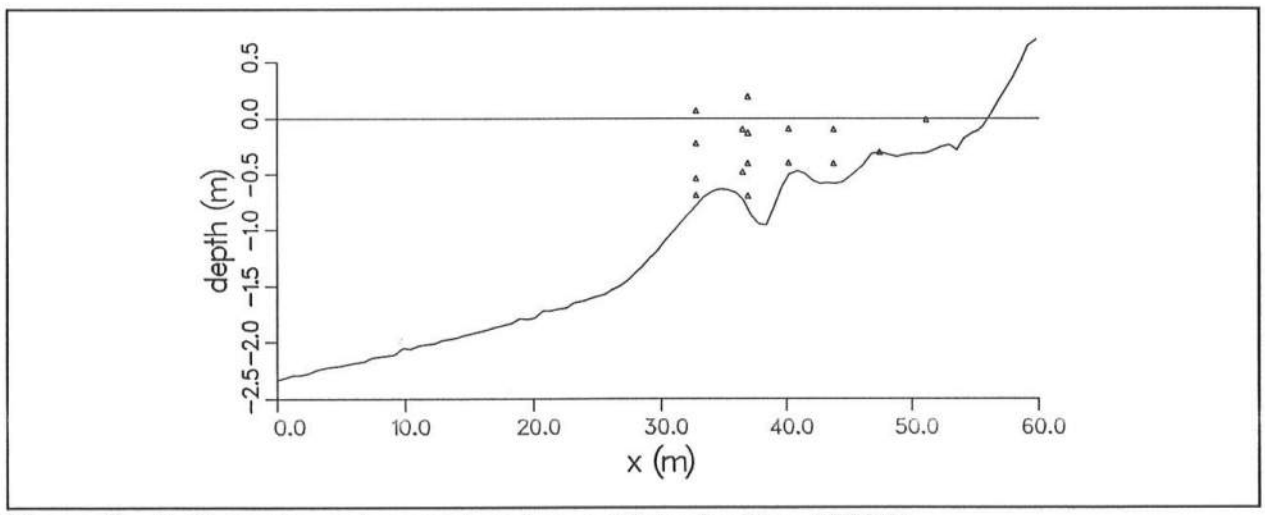

Figure 3. Bathymetry and current meter positions for Run A2007B

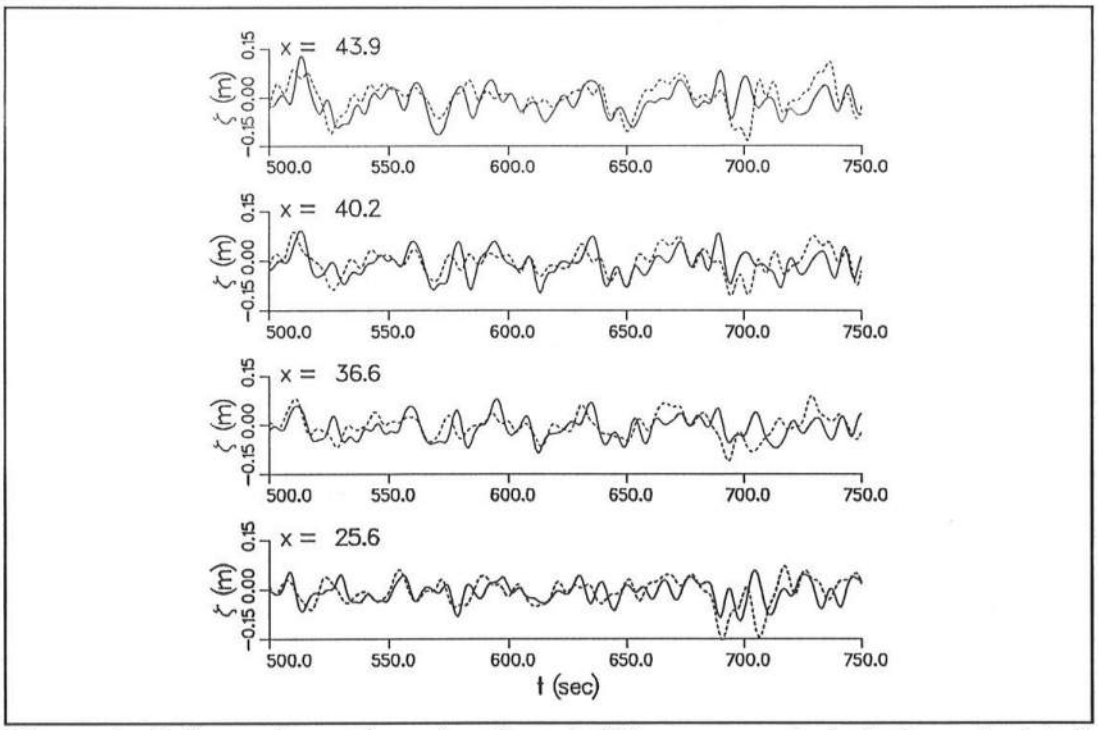

Figure 4. Infragravity surface elevations (solid -- measured, dashed -- calculated) for Run A0509A

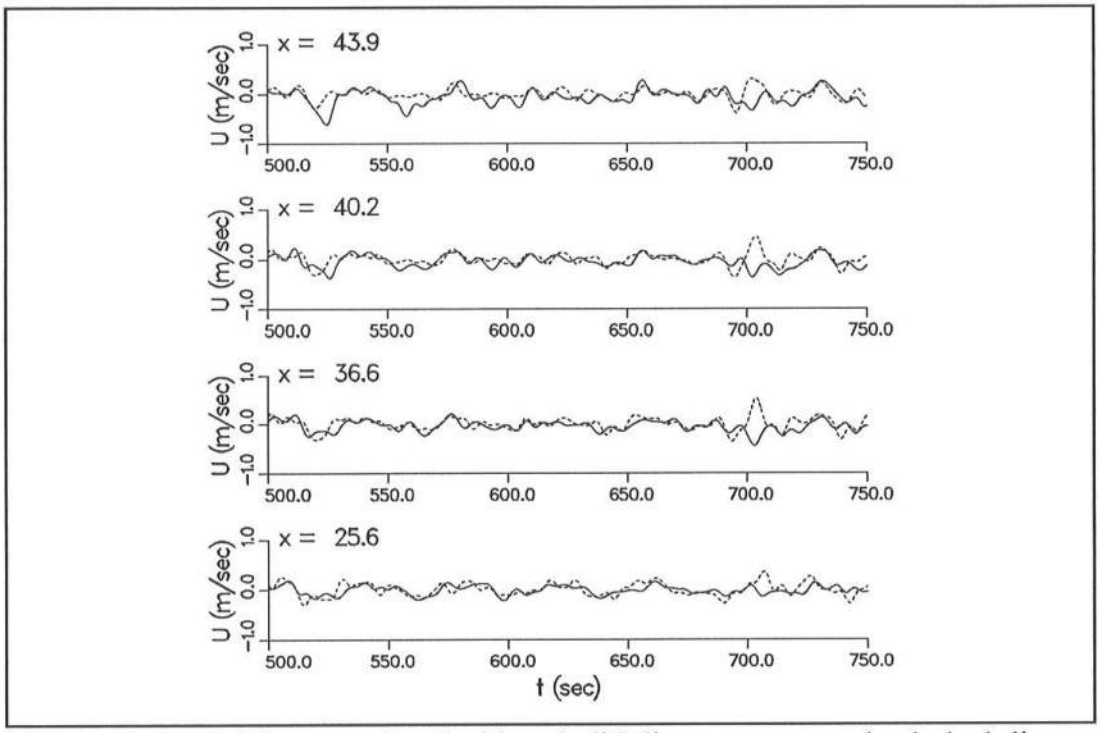

Figure 5. Depth-integrated velocities (solid line -- measured, dashed line -- calculated) for Run A0509A

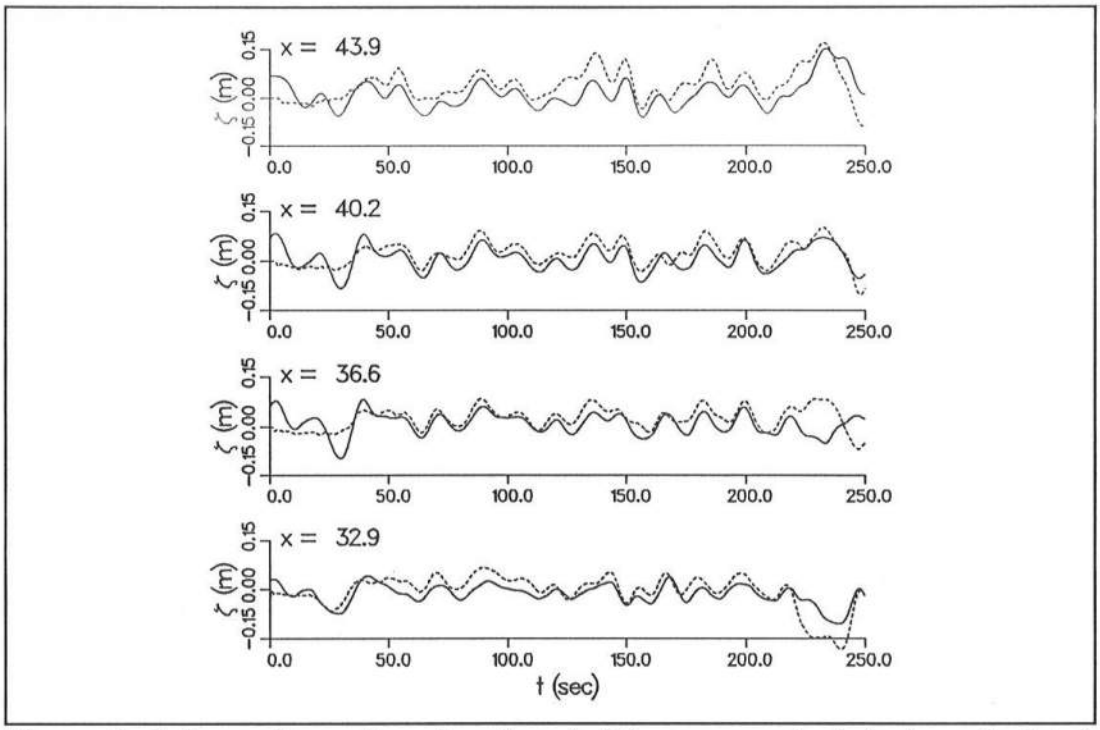

Figure 6. Infragravity surface elevations (solid -- measured, dashed -- calculated) for Run A2007B

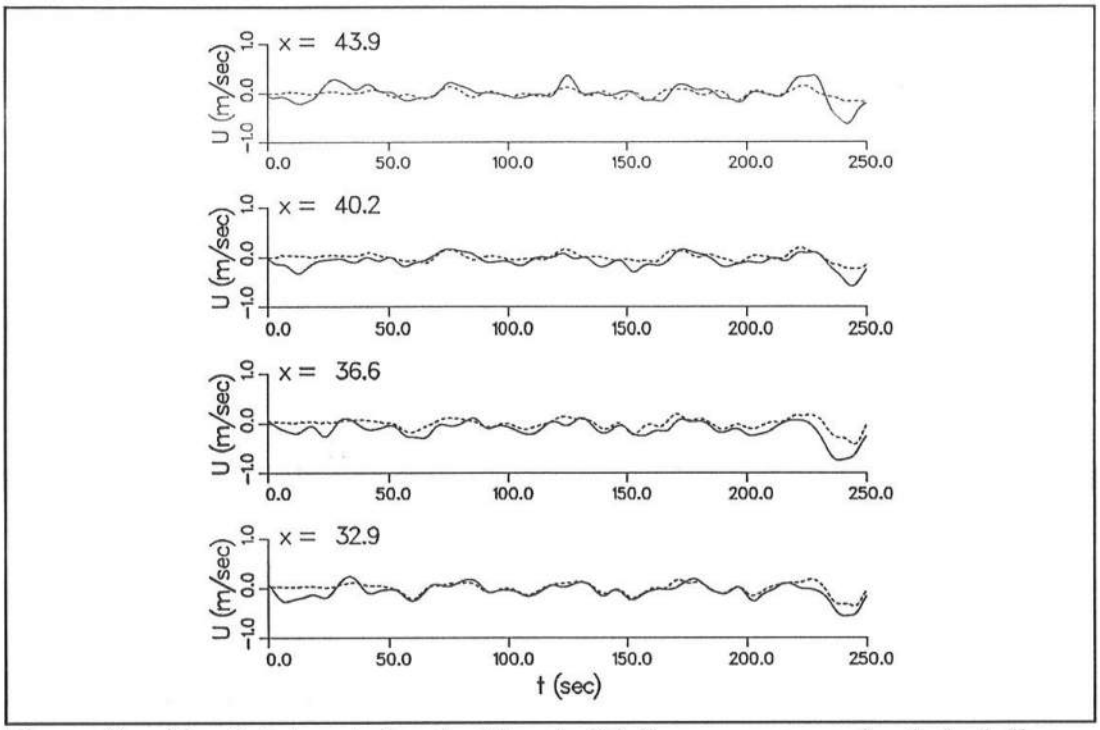

Figure 7. Depth-integrated velocities (solid line -- measured, dashed line -- calculated) for Run A2007B

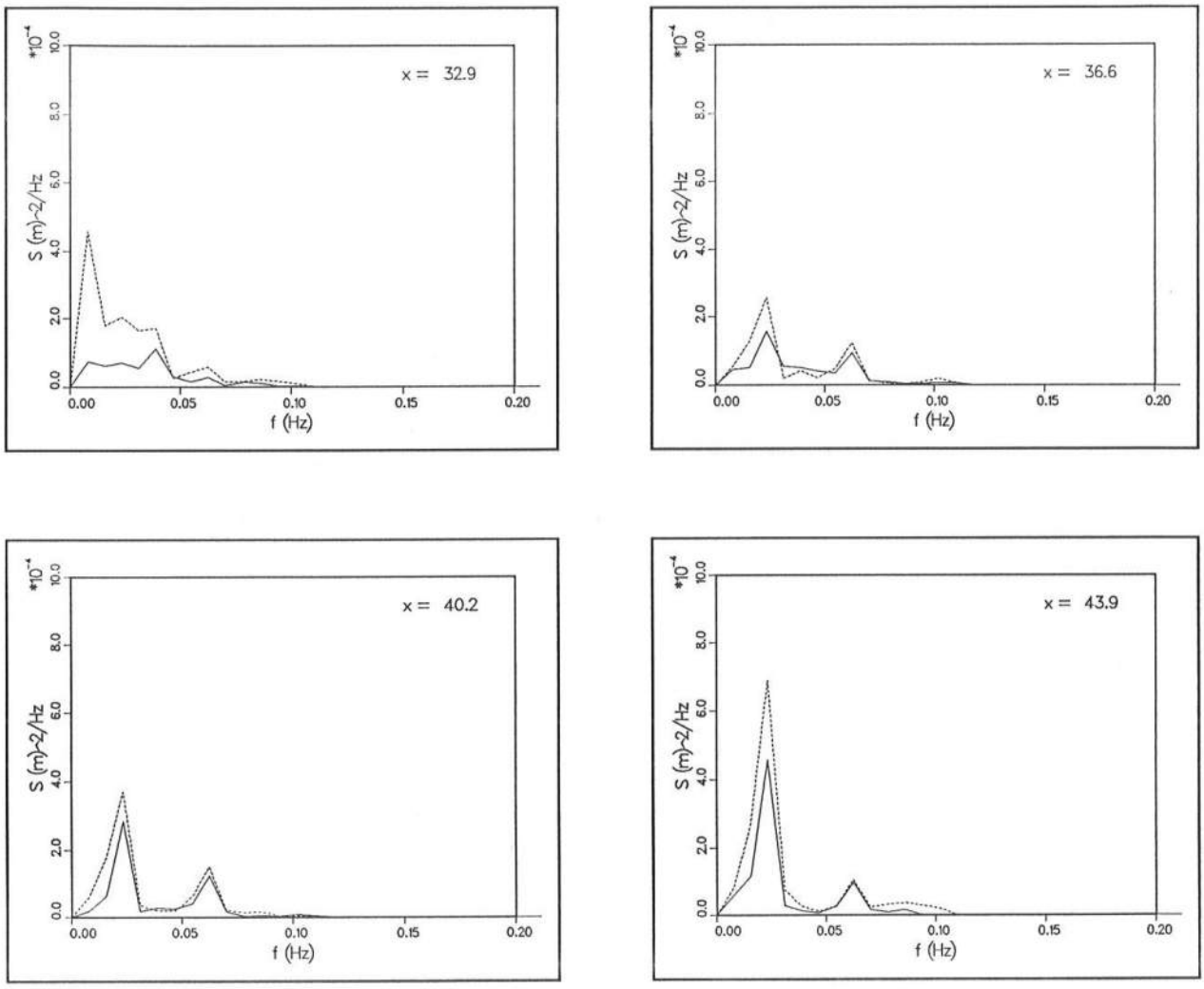

Figure 8. Spectra of infragravity-wave water surface elevations for Run A2007B.

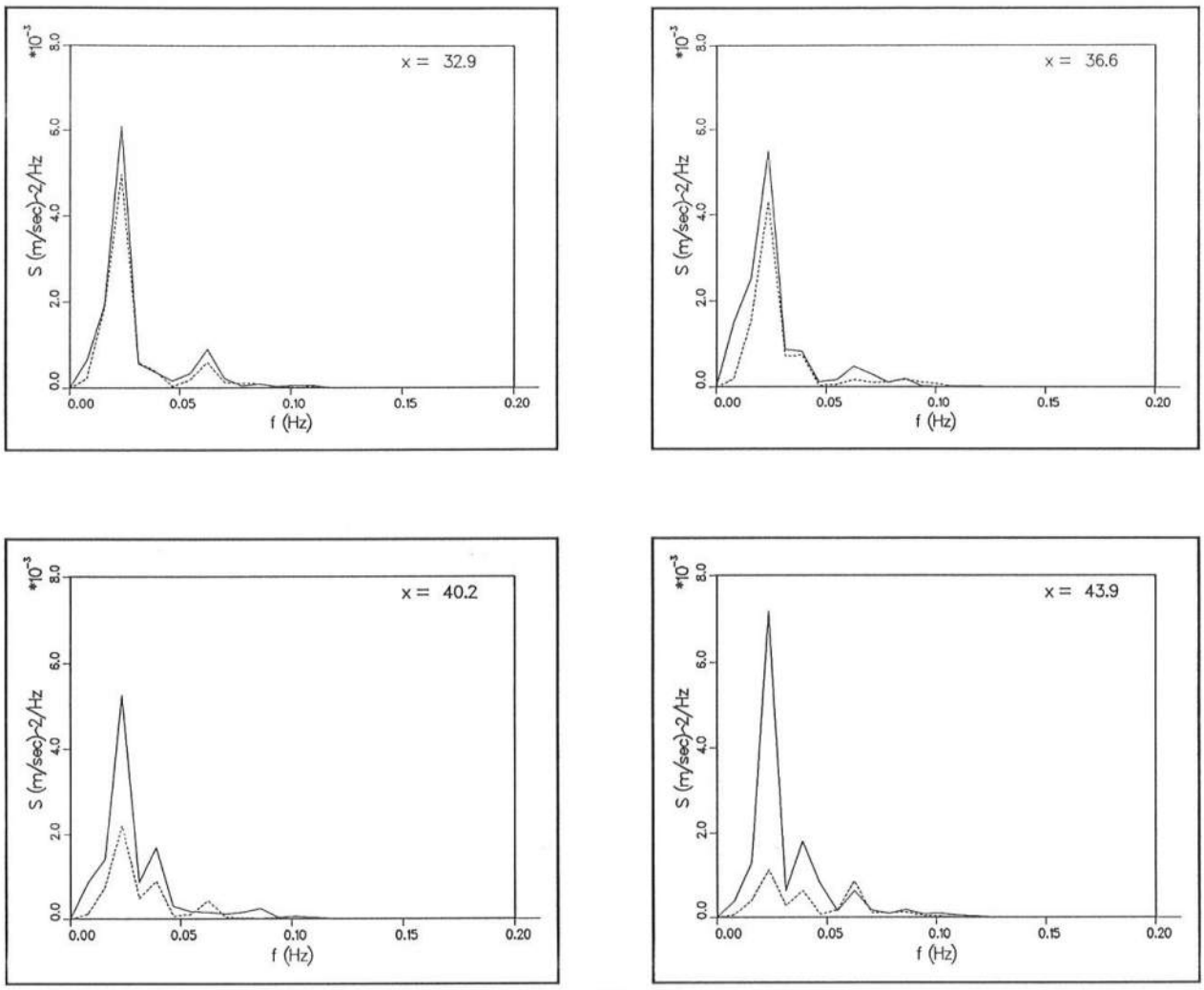

Figure 9. Spectra of infragravity-wave depth-integrated velocities for Run A2007B.

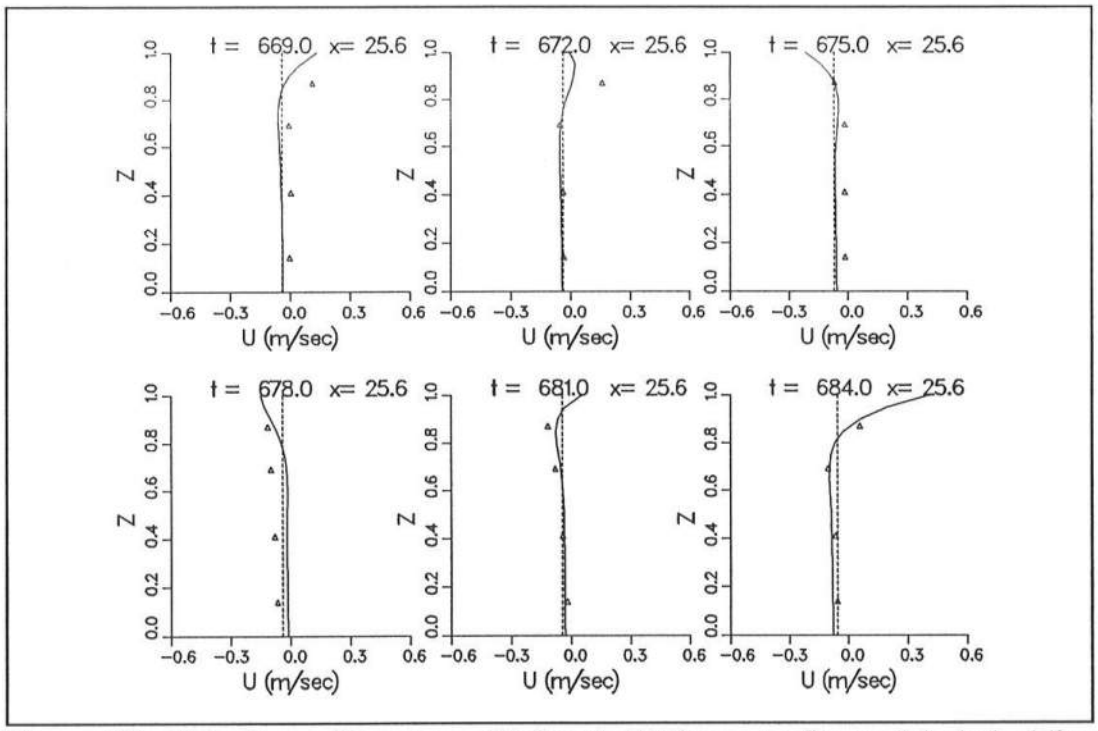

Figure 10. Velocity profiles at $x = 25.6$ m (solid line -- profile model, dashed line -- depth-integrated model, symbols -- measurements) for Run A0509A

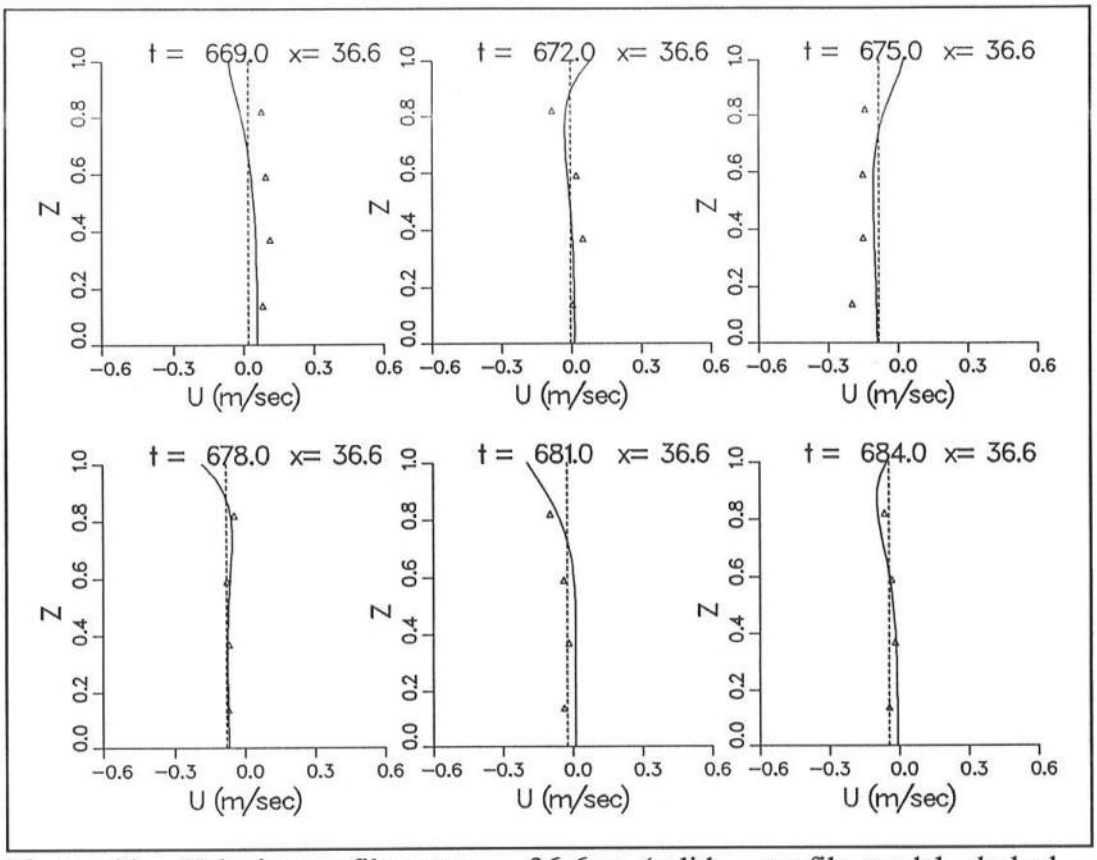

Figure 11. Velocity profiles at $x = 36.6$ m (solid -- profile model, dashed -- depth-integrated model, symbols -- measurements) for Run A0509A

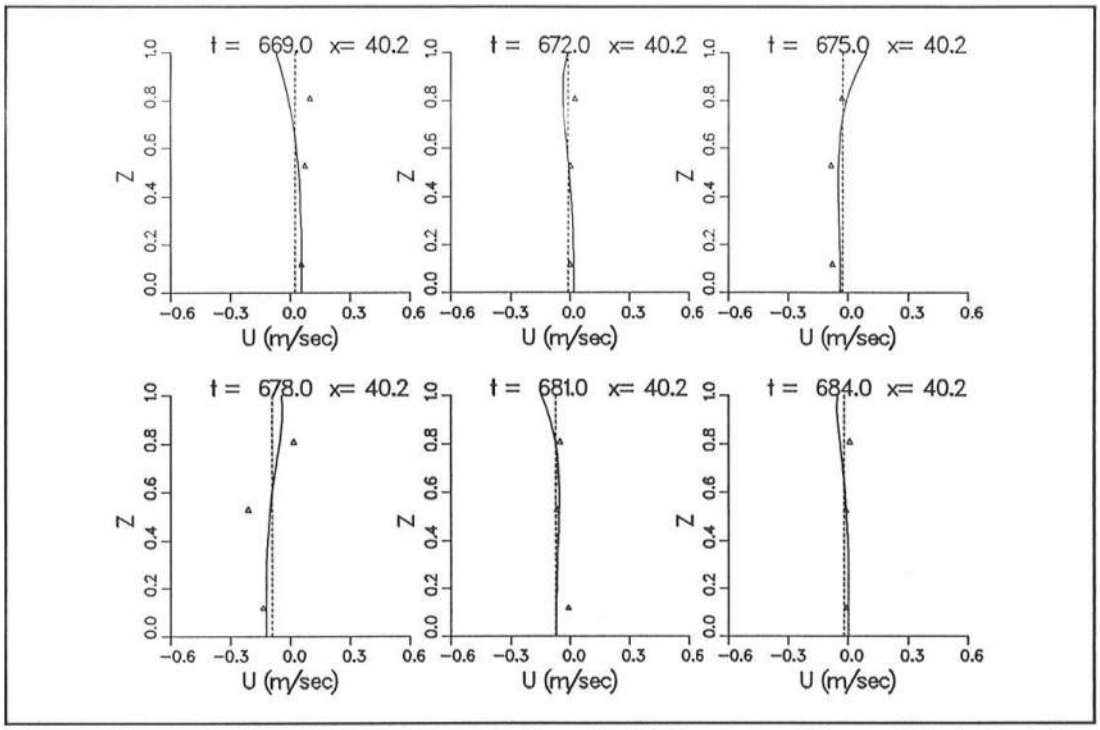

Figure 12. Velocity profiles at $x = 40.2$ m (solid line -- profile model, dashed line -- depth-integrated model, symbols -- measurements) for Run A0509A

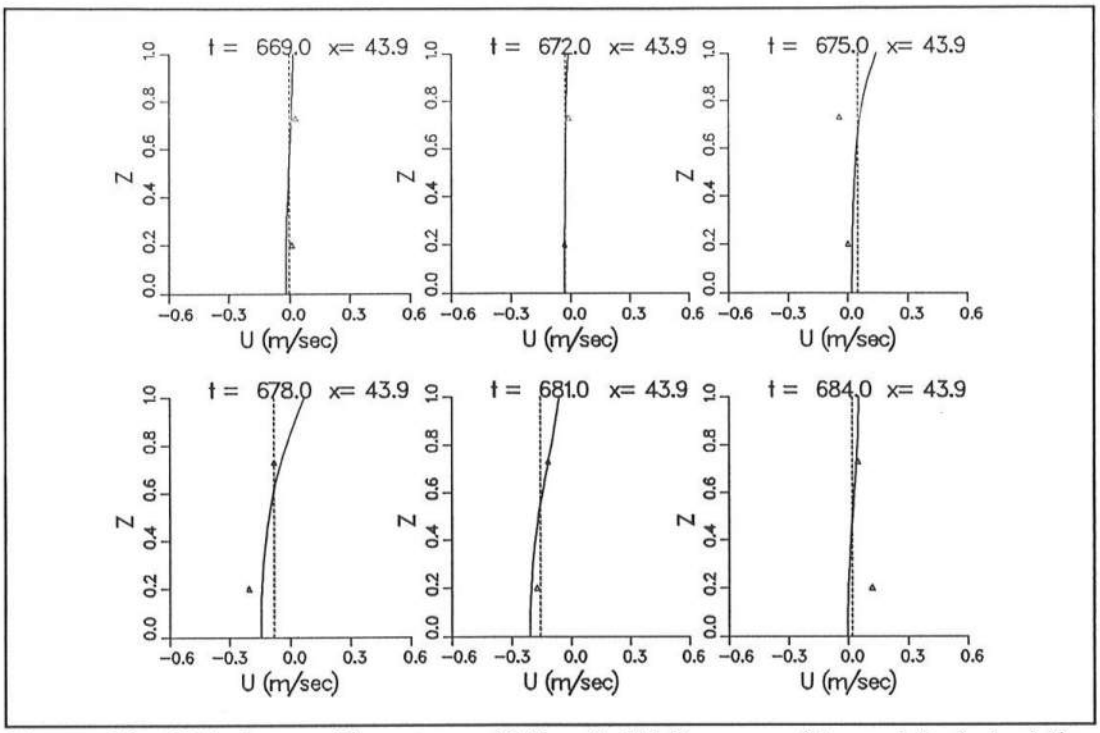

Figure 13. Velocity profiles at $x = 43.9$ m (solid line -- profile model, dashed line -- depth-integrated model, symbols -- measurements) for Run A0509A

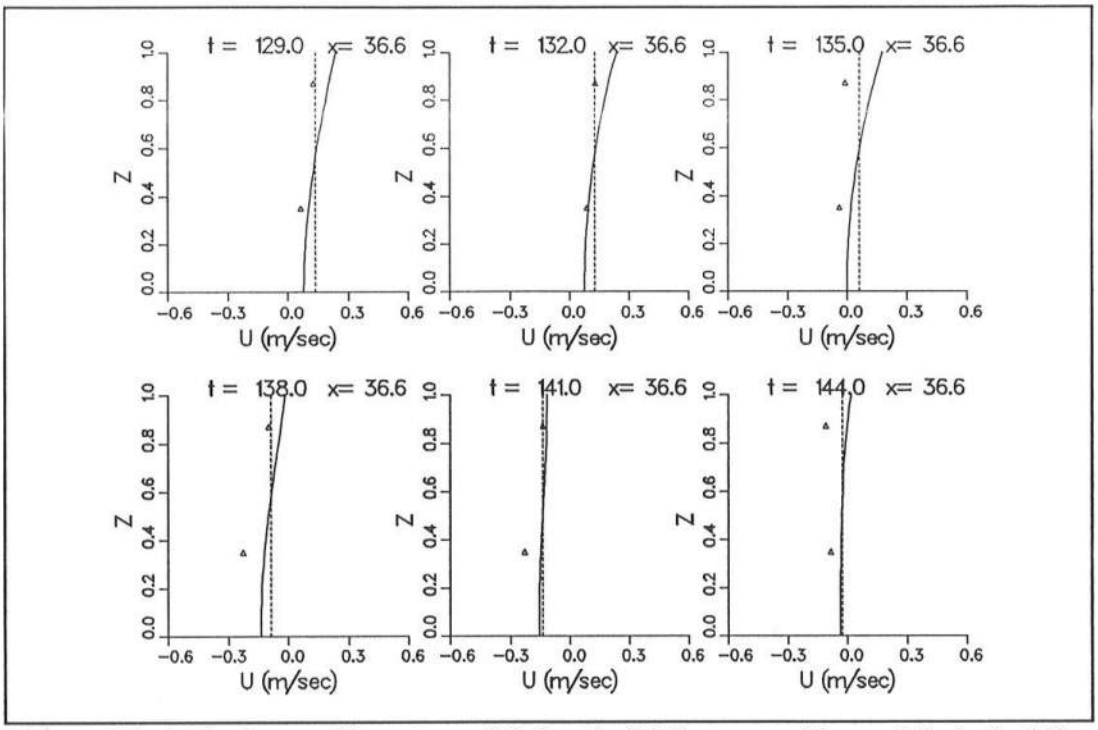

Figure 14. Velocity profiles at $x = 36.6$ m (solid line -- profile model, dashed line -- depth-integrated model, symbols -- measurements) for Run A2007B

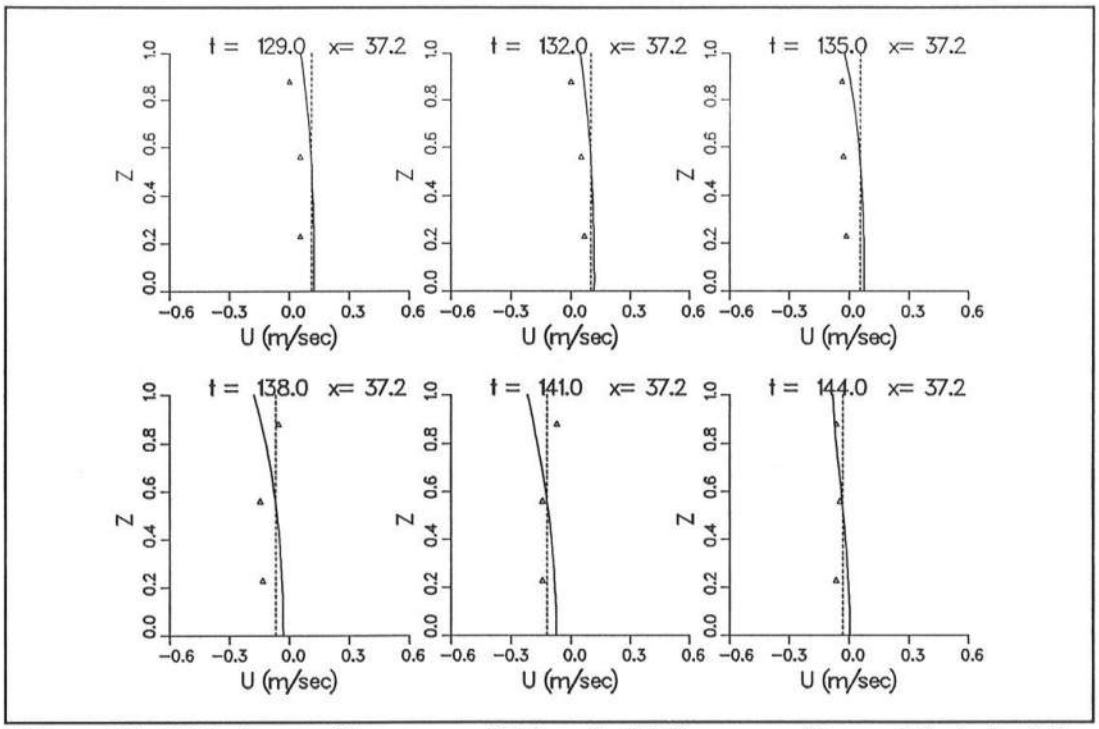

Figure 15. Velocity profiles at $x = 37.2$ m (solid line -- profile model, dashed line -- depth-integrated model, symbols -- measurements) for Run A2007B

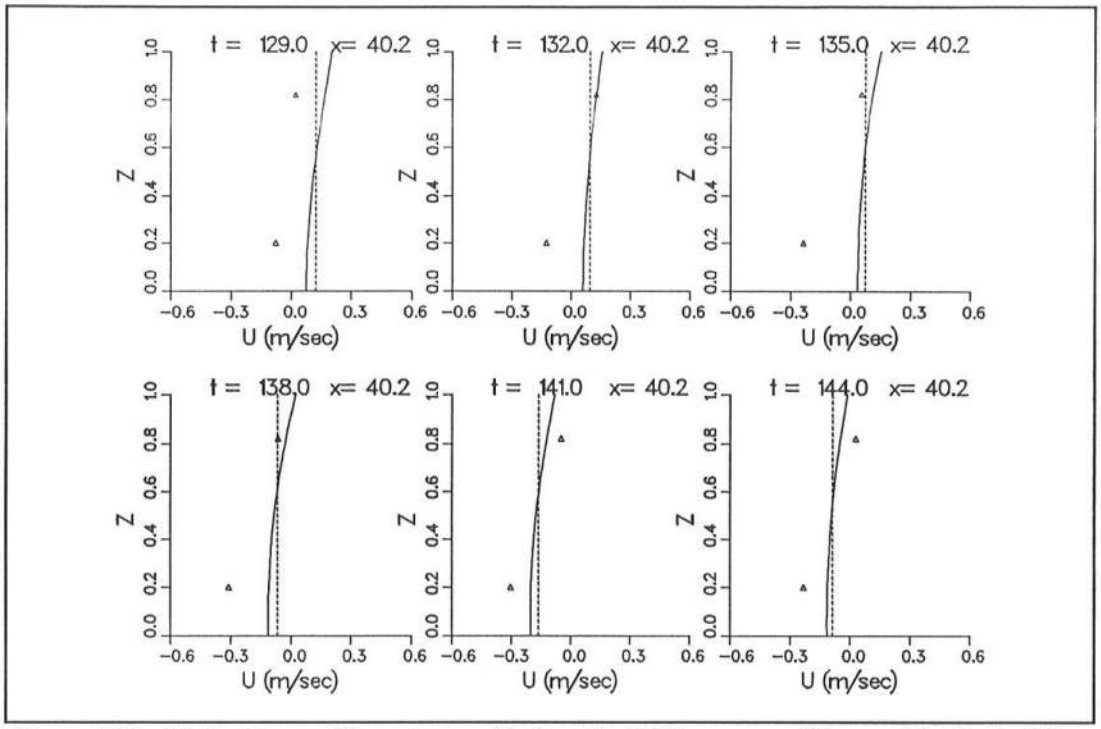

Figure 16. Velocity profiles at $x = 40.2$ m (solid line -- profile model, dashed line -- depth-integrated model, symbols -- measurements) for Run A2007B

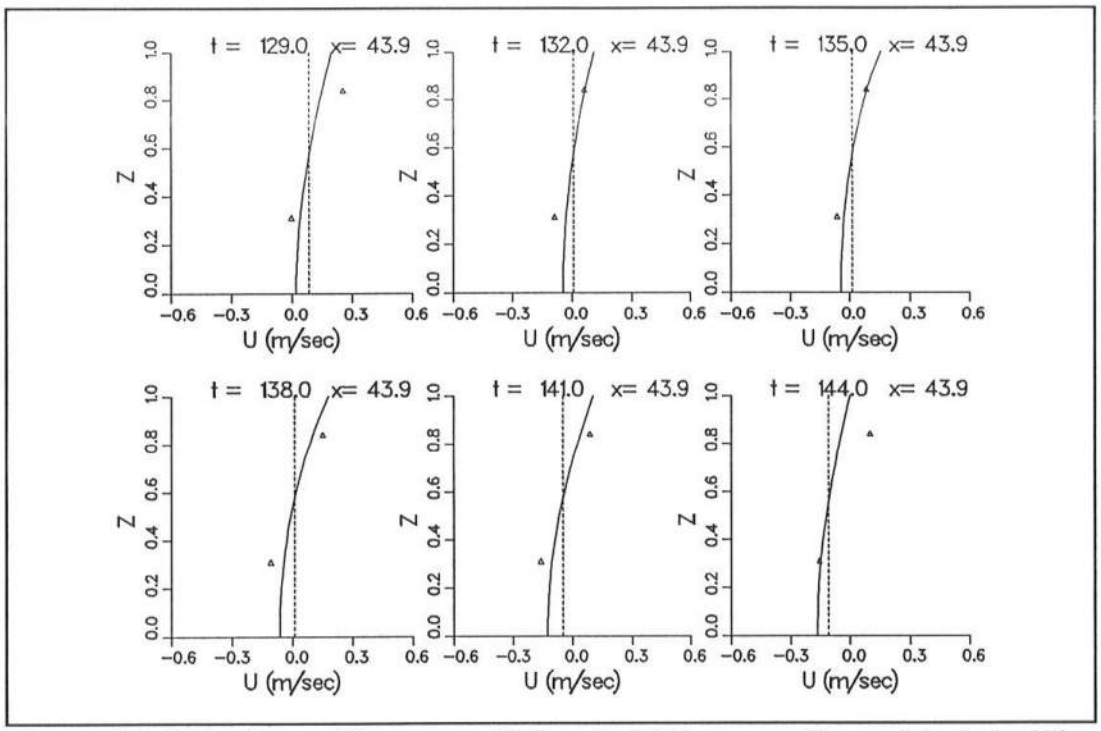

Figure 17. Velocity profiles at $x = 43.9$ m (solid line -- profile model, dashed line -- depth-integrated model, symbols -- measurements) for Run A2007B

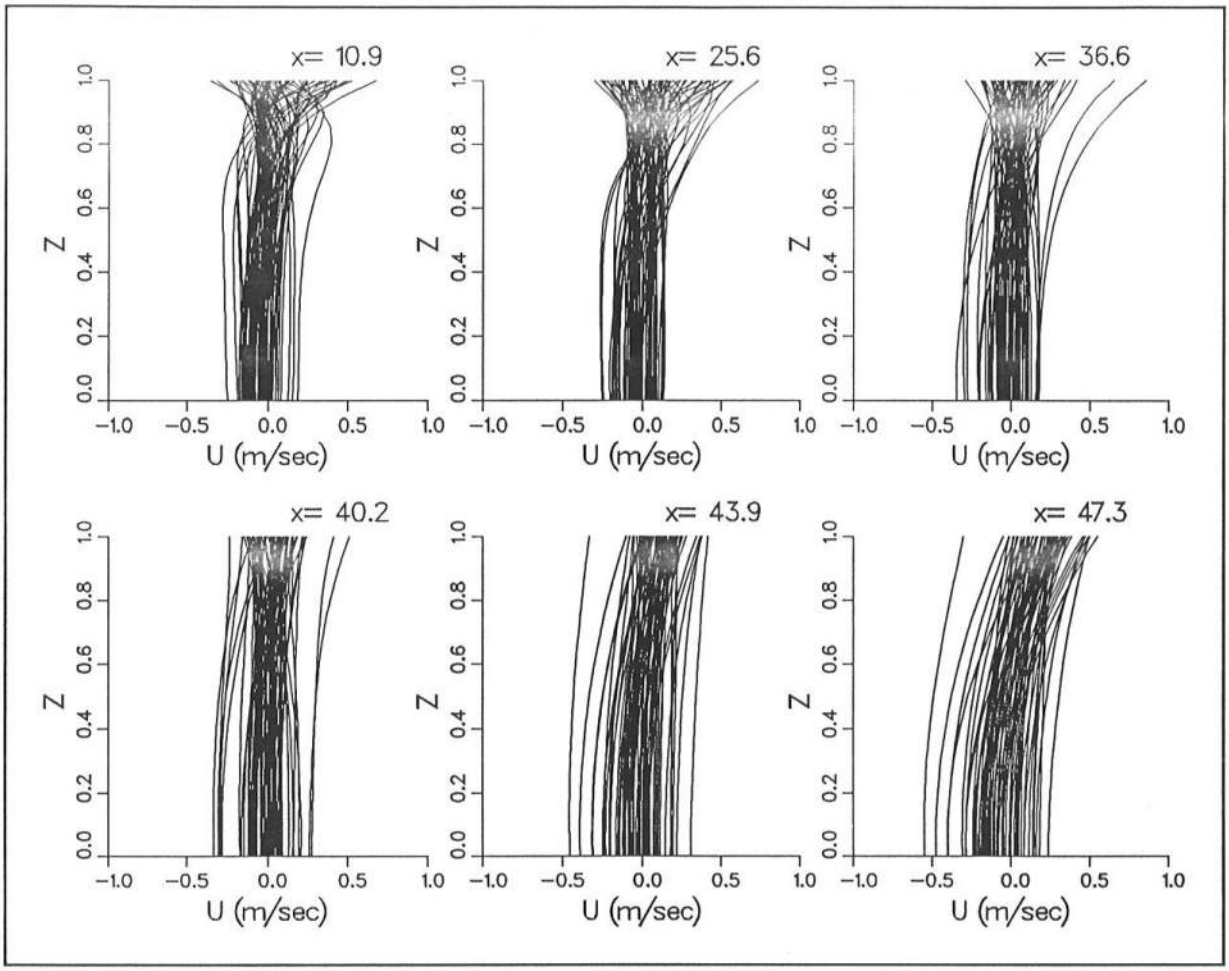

Figure 18. Calculated profiles for Run A0509A, t = 500-750 sec

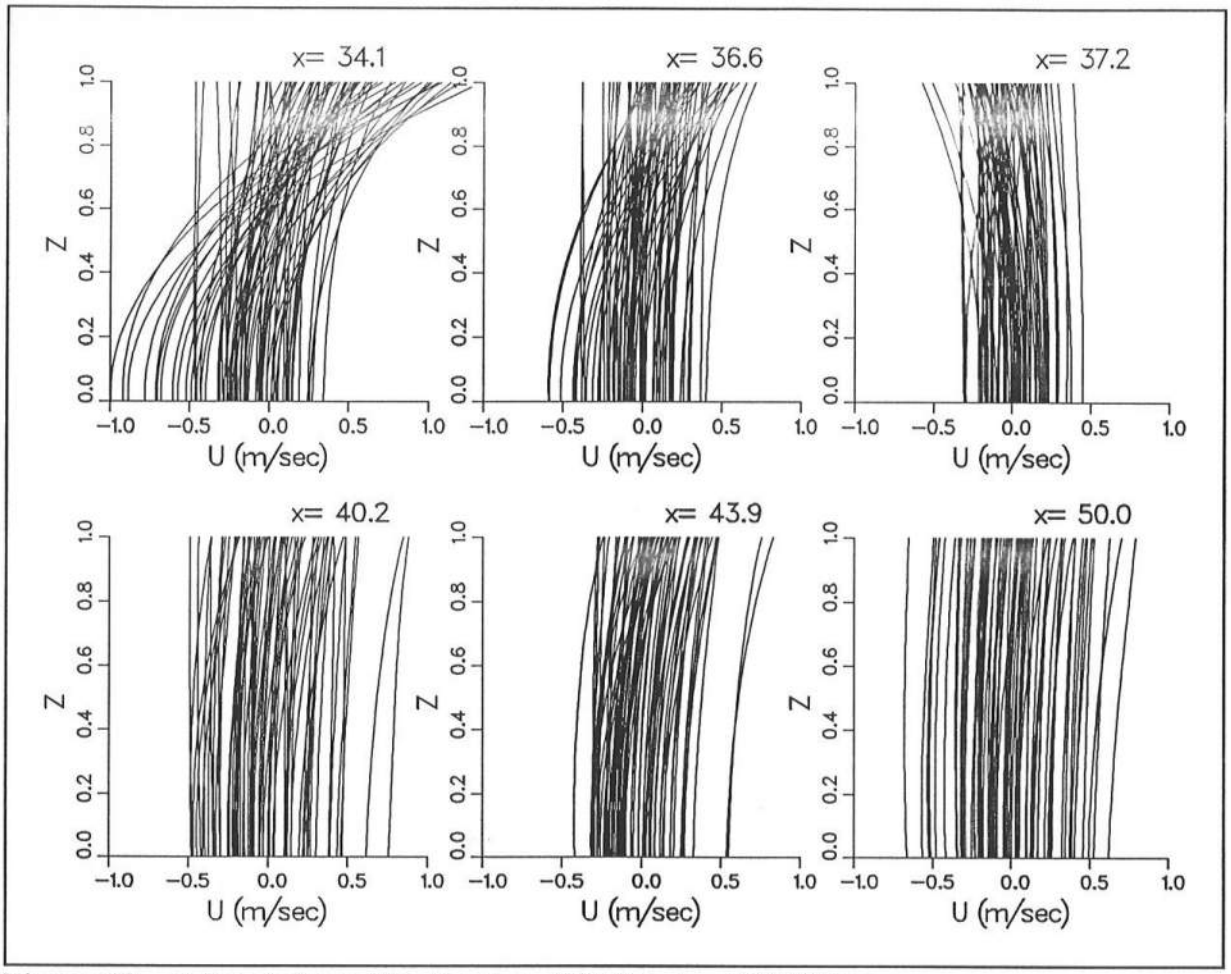

Figure 19. Calculated profiles for Run A2007B, t = 500-750 sec

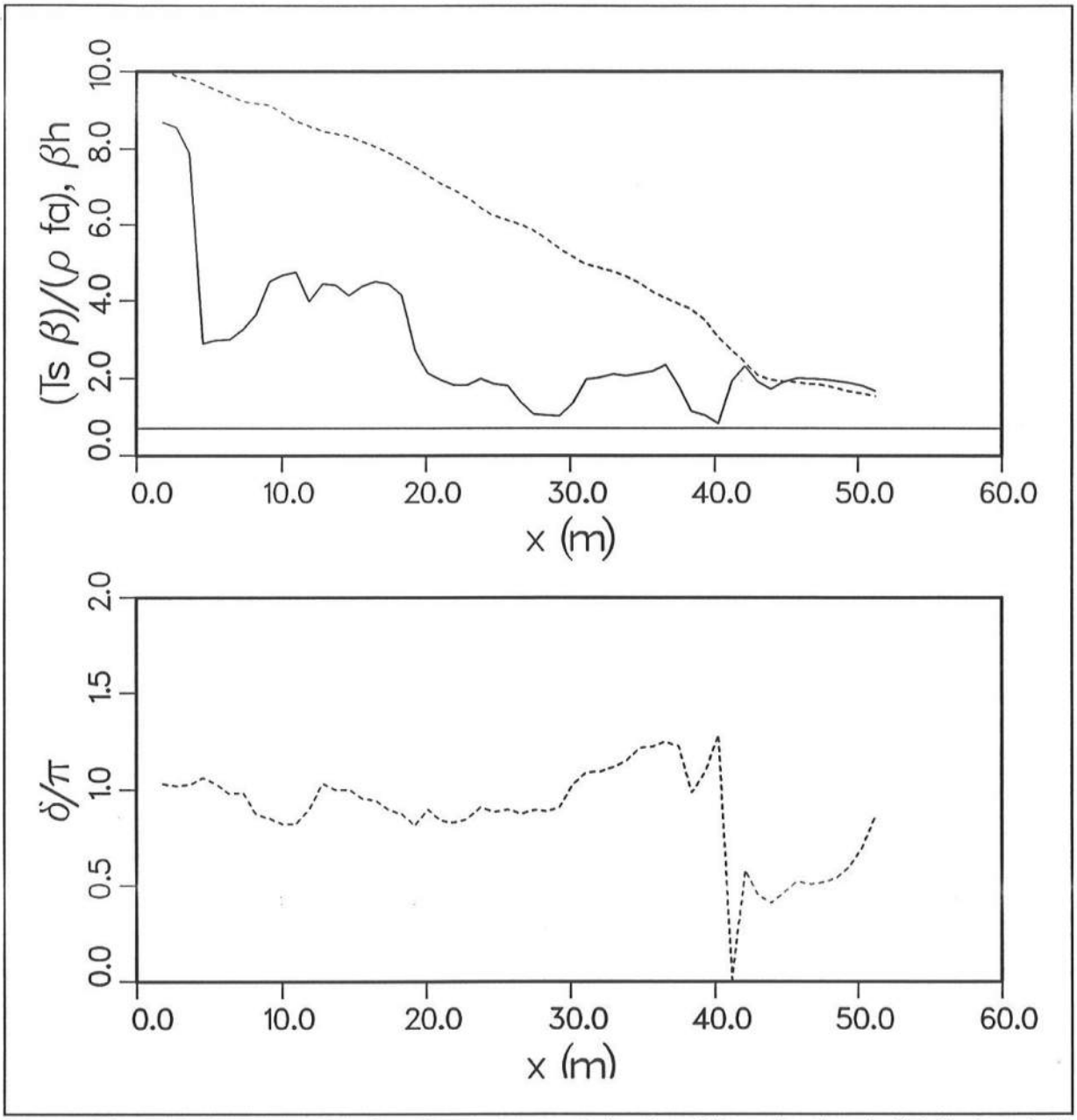

Figure 20. Relative strength of surface stress and depth-uniform forcing (solid line) and βh (dashed line) and relative phase of surface stress and depth-uniform forcing for Run A0509A

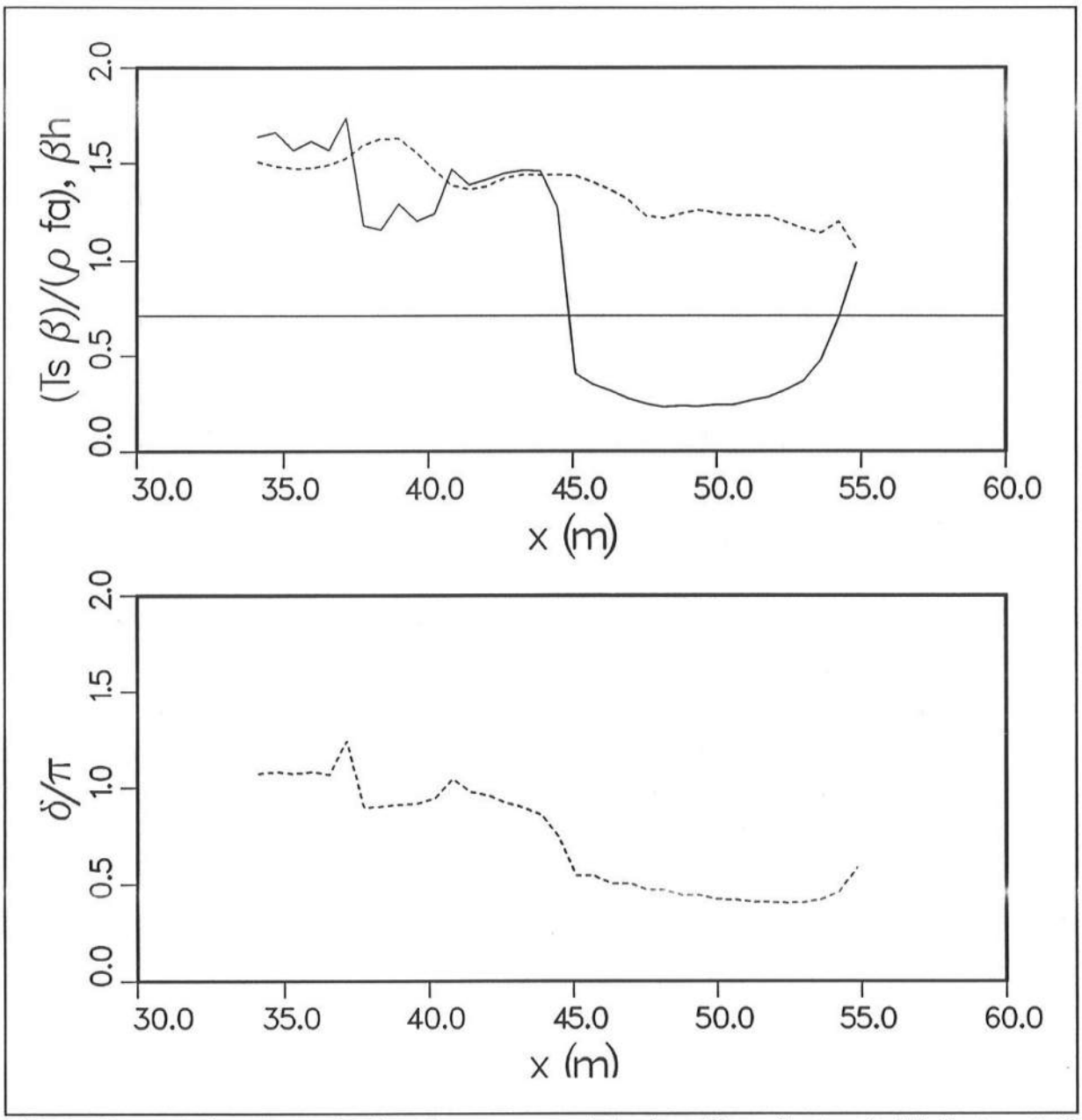

Figure 21. Relative strength of surface stress and depth-uniform forcing (solid line) and βh (dashed line) and relative phase of surface stress and depth-uniform forcing for Run A0509A